AERODYNAMIC TESTING OF A CIRCULAR PLANFORM CONCEPT AIRCRAFT

Except where reference is made to the work of others, the work described in this thesis is my own or was done in collaboration with my advisory committee. This thesis does not include proprietary or classified information.

_____
Bryan David Recktenwald

Certificate of Approval:

_____	_____
Roy Hartfield Professor Aerospace Engineering	Anwar Ahmed, Chair Associate Professor Aerospace Engineering
_____	_____
Gilbert Crouse Associate Professor Aerospace Engineering	Joe F. Pittman Interim Dean Graduate School

AERODYNAMIC TESTING OF A CIRCULAR PLANFORM CONCEPT AIRCRAFT

Bryan David Recktenwald

A Thesis

Submitted to

the Graduate Faculty of

Auburn University

in Partial Fulfillment of the

Requirements for the

Degree of

Masters of Science

Auburn, Alabama
August 9, 2008

AERODYNAMIC TESTING OF A CIRCULAR PLANFORM CONCEPT AIRCRAFT

Bryan David Recktenwald

_____
Signature of Author

_____
Date of Graduation

THESIS ABSTRACT

AERODYNAMIC TESTING OF A CIRCULAR PLANFORM CONCEPT AIRCRAFT

Bryan David Recktenwald

Masters of Science, August 9, 2008
(B.S., Aero. Eng., Auburn University, 2006)

86 Typed Pages

Directed by Anwar Ahmed

Auburn University has entered into collaboration with Geobat Flying Saucer Aviation Inc. for aerodynamic and flow visualization studies of the Geobat aircraft. The aircraft model that was tested consisted of a circular planform with a central opening.

A circular disk with an airfoil cross-section in the streamwise direction can offer distinct advantages of a circular planform configuration such as the reduced influence of tip vortices and hence lower induced drag. The aerodynamic challenges of such planforms include longitudinal and lateral stability, controllability and handling qualities partly due to the unique dynamics of wake vorticity.

Wind tunnel testing was conducted to study the longitudinal stability of the Geobat aircraft. Studies include analysis of both a solid flat disk and one with similar geometric characteristics of the Geobat. The Geobat was tested with and with out a

leading edge transition strip to determine the difference between laminar and turbulent flow over the model. Multiple flap and elevator deflections were tested for both cases to help determine longitudinal stability characteristics. For comparison, a highly stable and conventional aircraft model, a Cessna 172, was also tested under the same conditions.

After comparing, it was found that the Geobat model yielded much better stall characteristics than the Cessna 172 while pitching moment trends show a far less stable aircraft. Comparing the laminar and turbulent testing, aerodynamic data shows that the transition strip does not affect the longitudinal characteristics below the stall region. This illustrates that the flow over the model is already turbulent in nature. This can be seen in the flow visualization tests where a crescent shaped separation bubble was located at the leading edge tripping the flow to turbulent. Also distinct recirculation near the cockpit and trailing edge of the control surfaces was also observed.

ACKNOWLEDGMENTS

The author would like to thank Randy Pollard and Jack Jones of the Geobat Flying Saucer Aviation Inc. for their continued involvement during the research period. The author would also like thank Dr. Anwar Ahmed along with his committee for providing him with guidance and support.

Style manual or journal used:	Modern Language Association Style Manual
Computer software used:	Microsoft Office Word 2003 Microsoft Office Excel 2003 UGS Solid Edge V19 Labview V8.2 Tecplot 10

TABLE OF CONTENTS

NOMENCLATURE

α	Angle of attack, deg
α_{CDmin}	Angle of attack at minimum drag, deg
$\alpha_{L=0}$	Angle of attack at zero lift, deg
c.g.	Center of gravity
C_D	Drag coefficient
C_{D0}	Drag coefficient at lift = 0
$C_{D0\alpha}$	Minimum drag angle, deg
C_{Dmin}	Minimum drag coefficient
C_L	Lift coefficient
C_{Lmax}	Maximum lift coefficient
$C_{L\alpha}$	Lift-curve slope, $\frac{\partial C_L}{\partial \alpha}$
$C_{L\alpha=0}$	Lift coefficient at zero angle of attack
C_M	Pitching moment coefficient
C_{M0}	Pitching moment coefficient at zero angle of attack
$C_{M\alpha}$	Pitching moment curve slope, $\frac{\partial C_M}{\partial \alpha}$
ΔC_M	Change in pitching moment coefficient
δ_e	Elevator deflection, deg
δ_F	Flap deflection, deg
h	Center of gravity location, ft
h_n	Neutral point location, ft
K_n	Static margin, ft
L/D_{max}	Maximum lift to drag ratio
NP	Neutral point

LIST OF FIGURES

LIST OF TABLES

1 INTRODUCTION

1.1 Effects of aspect ratio

Unconventional aircraft of disk shaped planform configurations have been studied for several decades including the Vought V-173 (‘The Flying Pancake’) and the aircraft in this study, the Geobat. These disk shaped aircraft as well as most fighter aircraft have a very low aspect ratio wing designs. Aircraft with low aspect ratio wings behave differently than high aspect ratio aircraft, such as the USAF B52 bomber and sail planes. The aspect ratio, AR, is determined by the wing span, b, and the wing area, S, as shown in equation 1.1.

$$AR = \frac{b^2}{S} \qquad (1.1)$$

In comparison with high AR aircraft, low AR aircraft typically have higher structural integrity, are more maneuverable, have lower parasitic drag and better space efficiency. A large span wing will have to overcome a larger moment of inertia in order to roll therefore a lower AR will have a higher roll rate which is very important in fighter planes. Another advantage is the structural weight of a low AR aircraft. The larger the AR, the larger the wing bending moment at the wing root and therefore the stronger the wing structure has to be, increasing the weight of the aircraft. This increase in weight will affect the performance of the airplane. For example, the thrust required will increase which will increase the fuel consumption and reduce the range of the [1].

In designing an aircraft, the AR is one of the most important design features. It strongly affects the maximum lift to drag ratio at cruise conditions impacting the range of the aircraft [1]. Although low AR wings have advantage of higher roll rates and lower structural weight, there are other performance penalties, one being the increase in induced drag. Induced drag plays an important roll in determining the efficiency of the aircraft. Induced drag is a pressure drag that is a result of wing-tip vortices that induce changes in the velocity and pressure over the wing. These vortices induce a downward component of velocity called downwash, w, which causes an induced angle of attack, α_i, and results in the wing seeing an effective angle of attack, α_{eff}, which is smaller than the geometric angle of attack, α_g, as seen in Figure 1.1. Moreover, since lift is perpendicular to the local relative wind, the downwash tilts the lift vector aft and results in a component of lift in the drag direction. This is referred to as induced drag.

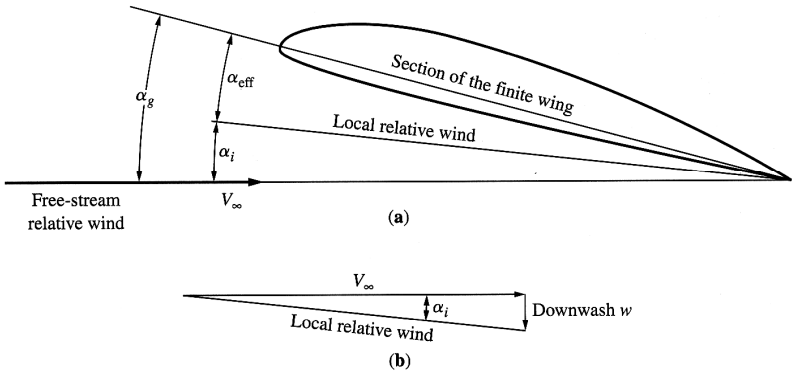

Figure 1.1 Illustration of induced and effective angles of attack [1]

As mentioned above, the downwash results in a lower C_L value at a given geometric angle of attack. Estimation of the aerodynamic coefficients for finite wings can be done by using Prandtl's lifting line theory. Using this theory, the lift slope for finite wings can

be written as shown in Equation 1.2, where a_0 is the slope for a given infinite airfoil and e is the span efficiency factor [2]. An elliptical lift distribution over the wing minimizes the induced effects and how close the lift distribution is to an elliptical shape is the span efficiency factor, e [1]. Most aircraft have an efficiency factor from 0.90 to 0.97 [1]. This equation will yield $a<a_0$ which shows that a higher aspect ratio wing will have a higher lift slope. The angle of attack at zero lift should be the same for any value of AR because the induced effects disappear at zero lift[1].

$$a = \frac{a_0}{1 + 57.3a_0/(\pi eAR)} \qquad (1.2)$$

The strength of the tip vortex decays with lateral distance from each vortex, creating a smaller induced drag for larger AR wings. This can be seen in Equation 1.3 where it is shown that increasing the aspect ratio will decrease the induced drag, C_{Di}. This induced drag value plays an important roll in the aircraft total drag found in Equation 1.4. The total drag is found by adding the induced drag to the profile drag which includes the friction drag and pressure drag of the aircraft.

$$C_{Di} = \frac{C_L^2}{\pi eAR} \qquad (1.3)$$

$$C_{Dtotal} = C_{Dp} + C_{Di} \qquad (1.4)$$

Small aspect ratio aircraft have been known to have pronounced lateral instability mainly due to a smaller moment of inertia as well as the taper of the wing [3]. A larger taper will lead to more unstable characteristics when compared to a low tapered wing with a high aspect ratio. Low aspect ratio wings typically also have more gradual stall

characteristics because the larger downwash they experience reduces the effective angle of attack seen by the wing and hence delays stalls to a higher geometric angle of attack [1].

1.2 Low aspect ratio aircraft

Dating back to the early 1940's, several disk shaped aircraft were constructed and tested for both personal and military applications. Based on a hand tossed model, Arthur Sack constructed a low aspect ratio circular planform aircraft (Figure 1.2) [4]. During takeoff tests, it was noticed that the control surfaces were in a lower pressure area behind the circular wing. After design changes, the aircraft eventually left the ground but immediately banked to the left, as the small span wing was too short to compensate for the engine's torque. This project was eventually scrapped.

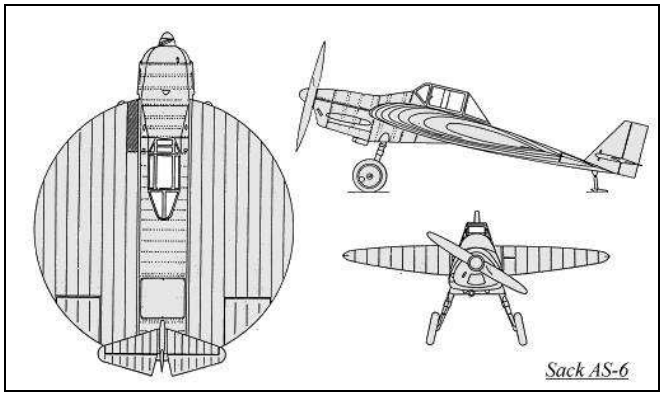

Figure 1.2 Schematic of the Sack AS-6 [4]

One of the most unusual aircraft ever designed for the U.S. Navy was the Chance Vought V-173, also known as the Zimmerman "Flying Pancake". It was a prototype

"proof of concept" aircraft that lacked wings, instead relying on its flat circular body to provide the lifting surface [5] (Figure 1.3).

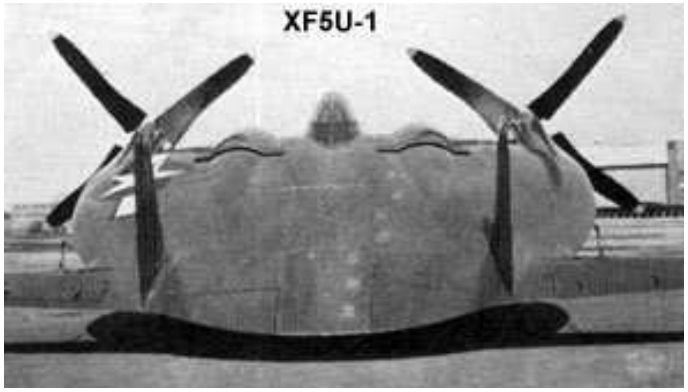

Figure 1.3 U.S. Navy's XF5U-1 [5]

As early as 1933, Charles Zimmerman had experimentally studied several airplanes with low aspect ratio wings and found a range of aspect ratios extending approximately from 0.75 to 1.50 wherein end flow caused a marked delay in the breakdown of the longitudinal flow as the angle of attack of the airfoil was increased [6]. He later determined from experiments that low aspect ratio wing designs were more efficient than conventional wings when the vortices from the wing were controlled with propellers [7]. With over a hundred flights starting in 1942, Zimmerman had successfully built a low aspect ratio aircraft known as the Vought V-173. Advantages of this aircraft included flying at very low speeds at large angles of attack as well as good maneuverability, both leading to a potentially safer form of flying [7]. Due to the introduction of jets, propeller-driven fighters became obsolete. Consequently the project was canceled and all work destroyed.

One of the more interesting configurations tested was a military concept called the Lenticular Reentry Vehicle or LRV (Figure 1.4). This was 'America's nuclear flying saucer' and was studied in the 1960's. Its design was considered because it created more lift than a standard wing, especially at low speeds, and provided more internal capacity for carrying bombs. This aircraft was proposed under classified research by the U.S. Air Force [8].

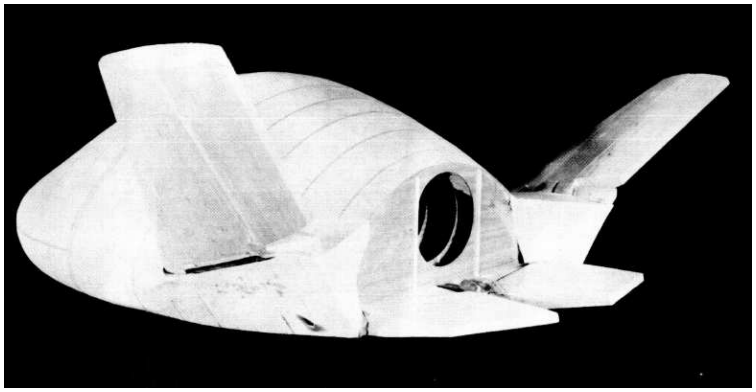

Figure 1.4 Wind tunnel model of the LRV [9]

The mission required orbital travel and the design allowed for bottom edge reentry into the atmosphere. Its disk form was designed to dissipate the heat of re-entry and later act as a wing. Its flattened tail structure was to provide directional stability and control. After testing several configurations in wind tunnels at subsonic speeds, it was found that the optimal LRV produced longitudinal stability, a positive pitching moment at zero angle of attack and a maximum lift to drag ratio of five. Although stable at lower angles of attack the LRV possessed unstable characteristics above 15 degrees angle of attack [9]. Although this aircraft never underwent flight testing, it was the U.S. Air Force's first flying disk aircraft.

Continued interest in circular planform aircraft has led to recent studies of Frisbees and flat disks of an aspect ratio of one. In the early 1970s the U.S. Navy commissioned a project in which the aerodynamic characteristics of a self-suspended Frisbee shaped flare was investigated [10]. Both spinning and non-spinning models were tested and it was found that spin had negligible effects on the aerodynamic forces and moments. Later, Stilley and Carstens [11] analyzed flight stability and compared actual flights to free-fall tests.

Several other wind tunnel investigations have been performed on circular disk configurations in the last 10 years. Mitchell [12] measured lift and drag on non-spinning disks. Yasuda [13] measured lift and drag for a range of flow speeds and spin rates for Frisbees and flat plates. Potts and Crowther [14] embarked upon many wind tunnel tests on disk shaped bodies. They not only measured the lift and drag but also pitching and rolling moments. Additionally they analyzed pressure distributions and air flow around the Frisbee and verified the results related to spin effects by Stilley [10]. Ali [15] performed comprehensive measurements of lift, drag and pitching moment for non-spinning disk-wing configurations and concluded that flat disk configurations posed concerns for longitudinal stability.

1.3 Problem statement

Jack Jones [16], a RC model airplane enthusiast, designed, built and flew a circular wing airplane named Geobat and declared it a “flying saucer.” Different views of this aircraft can be seen in Figure 1.5. Scaled flight tests showed excellent low speed handling qualities, nearly stall free landing and high alpha characteristics. A detailed

analysis of flight videos displayed a good overall performance envelope combining outstanding Short Take Off and Landing (STOL) performance and reasonably high cruise speeds with superb aerobatic capabilities [15].

Figure 1.5 Model views of the Geobat [15]

Even though this aircraft has been proven that it can fly under several RC configurations, there is still no aerodynamic data recorded on this aircraft. In order to further understanding this design, Auburn University has agreed to build an aerodynamic database for the Geobat aircraft through wind tunnel testing.

2 OBJECTIVES

Scaled flight tests of the Geobat showed flight characteristics that differed from a conventional aircraft configuration. The objective of this investigation therefore was to develop an experimental data base for further aerodynamic improvements and computational modeling of the Geobat aircraft using wind tunnel testing. This research focused on aerodynamic tests of the Geobat using a variety of flap and elevator deflections to help determine longitudinal stability characteristics. In addition, the model was tested with and without a leading edge transition strip to determine any differences between laminar and turbulent cases.

For further understanding of the Geobat, a solid disk, a flat disk of similar planform to the Geobat and a conventional Cessna 172 aircraft were tested and compared. Flow visualization was also conducted to show any flow trends that the aerodynamic data could not present.

3 WIND TUNNEL MODELS

3.1 The Geobat

3.1.1 Description

Two Geobat models were made available to Auburn University for wind tunnel testing.

The models had a disk-shaped body of 22 inch outer diameter with a central opening. The model can be best described as a joined wing with a circular arc rearward-swept front wing, a forward-swept rear wing with a circular trailing edge and two connecting wing tips, thus creating a 360 degree circular planform. The control surfaces included flaps, rear ailerons, a large elevator and two rudders. Each section of the Geobat was contoured with NACA 230xx series airfoil geometry. The nominal thickness was 12% but was varied, decreasing slightly in thickness moving away from the centerline. Key geometric characteristics of the model are presented in Table 3.1.

Table 3.1 Geobat geometric parameters

	Geobat model
Airfoil Section	NACA 230xx
Span, b (ft)	1.830
Chord, c (ft)	0.820
Wing area, S (ft^2)	1.320
Aspect Ratio, AR	2.530
C.G. loc. From nose (ft)	0.645

Figure 3.1 shows a top schematic view of the Geobat. The black sections are the flaps and elevator control surfaces. The gray sections signify the rear ailerons and the rudders.

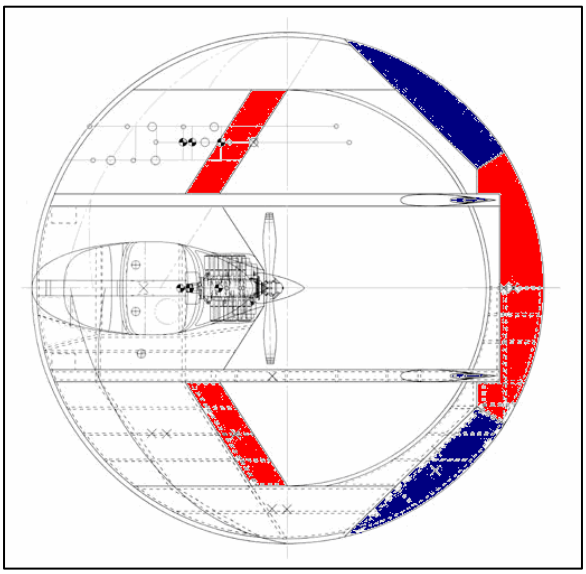

Figure 3.1 Top schematic of Geobat

3.1.2 Model preparations

The center of gravity was first determined for mounting on the wind tunnel balance. This was done by balancing the model on a point and verifying it with the c.g. location found in Figure 3.1. A counter sunk area was milled out around the model's c.g. This created a flat surface where four wood screws were used to secure the model to the mounting bracket, as well as decreased the flow interference created by the bracket (Figure 3.2).

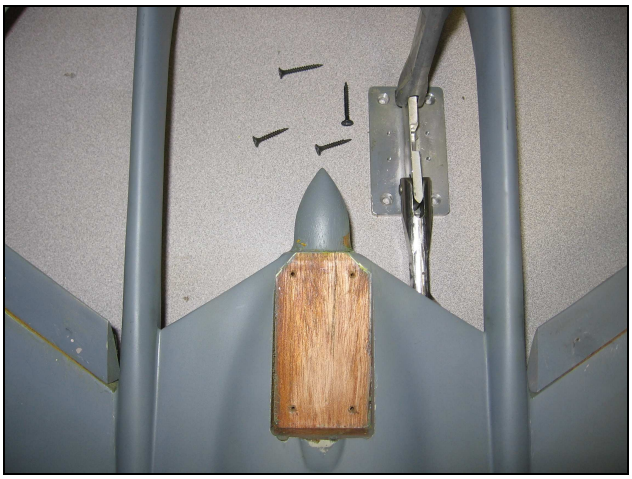

Figure 3.2 Geobat mounting location and mount

The primary model was modified so that the flap and elevator control surfaces could be attached and deflected. Flap settings consisted of 0, 10 and 20 degrees and the elevator was modified to deflect at ± 0, 10 and 20 degrees. The control surfaces hinged from the top surface of the model with two brackets (one set for each control surface). These brackets were installed flush with the model surface to prevent any disturbances in the flow. A total of 3 sets were made for the flaps and 5 sets for the horizontal stabilizer.

The brackets were made from aluminum stock 1/10 of an inch thick and an overall length of 1.5 inches and a width of 0.4 inches. The brackets were bent at their center, length wise. Two screw holes were drilled, 3/8 inches on either side of the bend and countersunk to accommodate a 4-40 hex screw. Each end was rounded off with a 1/4 inch radius.

Each control surface utilized two brackets. With the use of a rotary tool and guide line, each bracket location on the model was countersunk 1/8 of an inch so that once the bracket was in place it would be slightly below the model's surface. Brackets with 0 deg

deflection were then placed in each location and a through hole was drilled in the model at the bracket hole locations.

At the through hole locations on the underside of the model, blind nuts were countersunk to accept the hex bolt. Once set, they were glued in place, covered with adhesive filler and sanded down flush to the underside of the model. Figure 3.3 shows the hardware and detached rear elevator and Figure 3.4 shows the attached elevator with deflection.

Figure 3.3 Elevator hardware construction

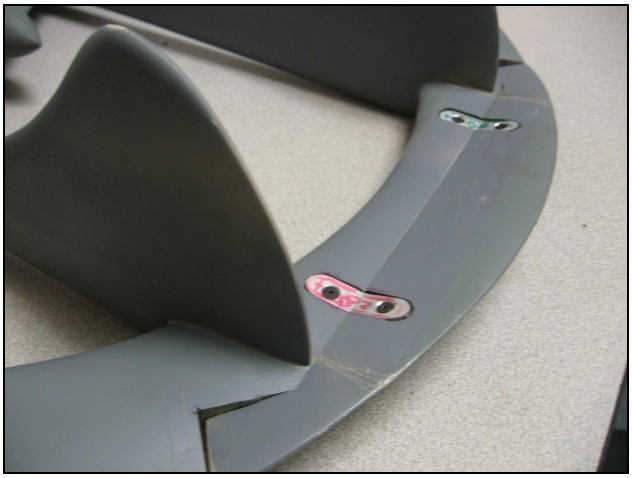

Figure 3.4 Attached elevator with hardware

During all tests the brackets and joints were covered with clear tape to minimize leakage and to maintain smooth flow.

3.1.3 Transition strip

For turbulent flow testing, a transition strip was installed on both the upper and lower surface of the front 10% of the airfoil. This was done by using a spray adhesive and coating 120 grit powder on top of it (Figure 3.5 and Figure 3.6).

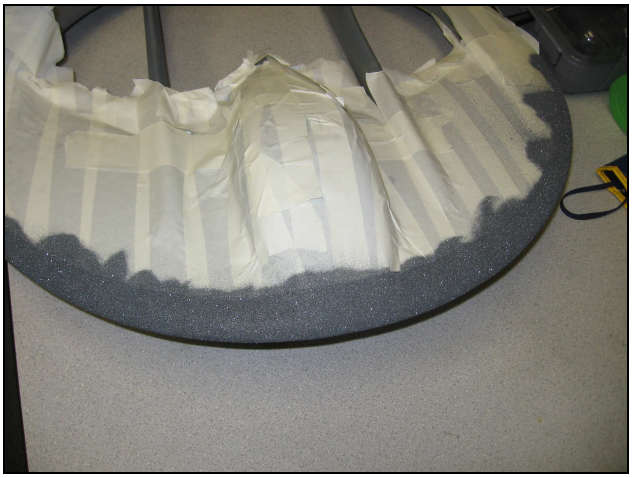

Figure 3.5 Application of transition strip

Figure 3.6 Final transition strip

3.2 Flat disks

For comparison purposes two additional flat disk models were constructed and tested. Both flat plates were 22 inches in diameter and 3/16 inches thick.

The first plate, (Figure 3.7) was a solid flat plate with a 45 degree chamfer on the all the edges of the model. Four tapped holes were drilled at the center of the model at the c.g. location for mounting purposes which was located in the center of the disk, 11 inched from the leading edge.

The second plate, (Figure 3.8) had a cutout which resembled the geometry of the Geobat model and had a 45 degree chamfer on all edges. Four tapped holes for mounting were located at the models c.g, 7.8 inches from the leading edge.

These plates were painted with a flat black primer in order to obtain flow visualization results with florescent dye.

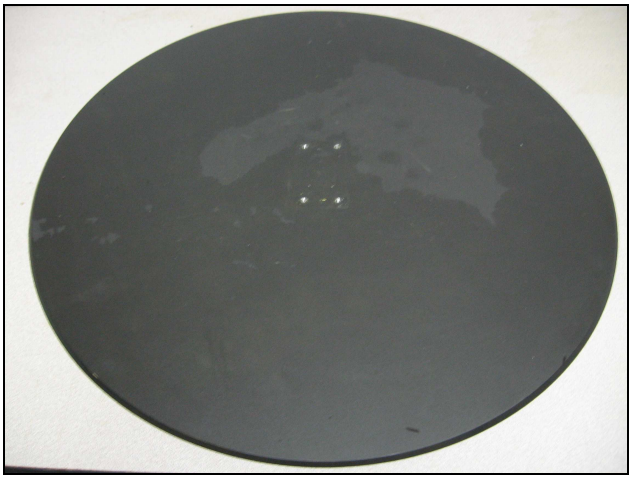

Figure 3.7 Flat solid disk model

Figure 3.7 Flat cutout disk model

3.3 Cessna 172

A Cessna 172 model was chosen for comparison to the Geobat for several reasons. The Cessna 172 is known to be a very stable aircraft through the entire range of angles of attack and its stability characteristics are well document. Both models have comparable attributes including similar gross weight. The Cessna 172 is a 4 person aircraft while the Geobat is designed as a two passenger aircraft. Table 3.2 lists the geometric features of the Cessna 172 model where Figure 3.9 shows the model that was used for aerodynamic testing. Flaps and elevators were deflected in the same ranges as the Geobat model.

Table 3.2 Cessna 172 geometric parameters

	Cessna 172 model
Airfoil Section	Clark Y
Span, b (ft)	2.500
Chord, c (ft)	0.375
Wing area, S (ft^2)	0.940
Aspect Ratio, AR	6.650
C.G. loc. From nose (ft)	0.585

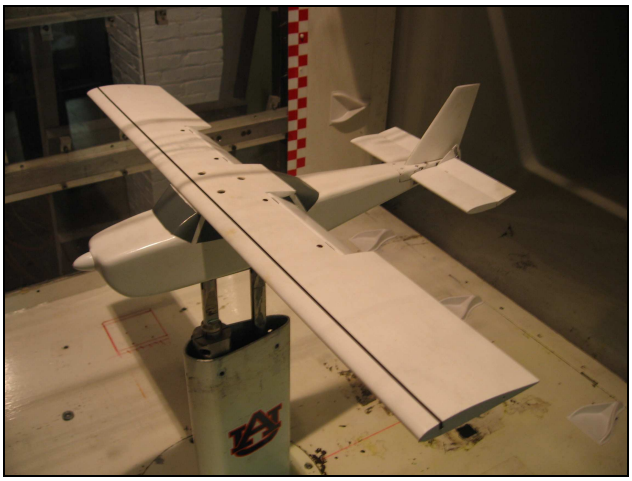

Figure 3.9 Cessna 172 wind tunnel model

4 EXPERIMENTAL SETUP

4.1 Description of test facility

Experiments were conducted in the Aerospace Engineering 3 ft x 4 ft cross-section wind tunnel. This is a closed loop, low subsonic tunnel capable of producing a maximum velocity of 180 ft/s. Force and moment data were acquired from a 6 component external pyramidal balance, (Figure 4.1) with the help of a National Instruments A/D board and Labview data acquisition software.

4.2 Test methods

4.2.1 Force and moment

Data was acquired at a sampling rate of 500 hertz. The raw data consisted of 2 second or 1,000 samples which were later processed through an in-house developed Labview program and stored in coefficient form. For each test, the angle of attack ranged from -5 to 20 degrees in 1 degree increments. A typical test setup including the wind tunnel, model and pyramidal balance is shown in Figure 4.2.

The pyramidal balance and the angle of attack potentiometer were calibrated before and after each series of tests. Calibrations checks were performed on a regular basis to check for any drift or hysteresis effects, however no such trends were observed. Prior to each test where a model experienced a change in weight or a slight c.g. movement, the

model had to go through an initial tare calibration allowing the weight of the model to be subtracted during data acquisition.

Tests were conducted at 70, 100 and 130 ft/s with corresponding Reynolds numbers of 330,000, 460,000 and 600,000 based on the Geobat chord of 0.820 ft. The flat disk models did not have any control surface deflections. The Geobat and Cessna 172 models were tested through a range of flap deflections of 0, 10 and 20 degrees and elevator deflections of ± 0, 10 and 20 degrees. The Geobat model was tested both with and without the leading edge transition strip. The Cessna 172 had a transition strip installed at the ¼ chord for the entire span of the wing.

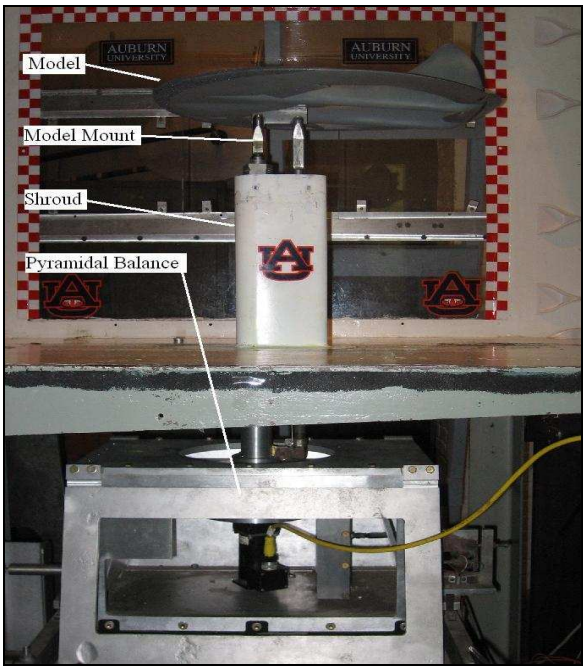

Figure 4.1 Wind tunnel test setup

4.2.2 Wind Tunnel Flow Visualization

Surface flow was visualized using powdered yellow fluorescent dye mixed in engine oil and a small quantity of oleic acid. This mixture was evenly brushed on the top surface of the model. All tests were conducted at 100 ft/s or a corresponding unit Reynolds number of 550,000. Once the air flow was established at the test speed, the resulting pattern of the limiting streamlines was illuminated with a UV light and photographed. These tests were conducted at -5, 0, 5, 10, 15 and 20 degrees angle of attack.

5 RESULTS AND DISCUSSION

5.1 Uncertainty analysis

After each balance calibration, a calibration check was done through an in house Labview program which checked strain gauge reliability. For all forces and moments, it was found that the largest error was 2%. The mean velocity of the tunnel varies within 5% of its true value. Noise introduced to the system was not measured and therefore not included in the analysis.

Prior to all testing, flow angularity of the tunnel was measured and found to be angled 2 degrees at the beginning of the test section in the vertical plane. Boundary layer transition strips were placed at the leading edge of the test section as well as vortex generators being placed at the tail end of the test section. With this addition, the flow was smoothed and the angularity was dropped only slightly, just below 2 degrees.

5.2 Geobat aerodynamic data

For the range of Reynolds numbers tested the data followed similar trends and magnitudes. Data presented in this text correspond to a freestream velocity of 100 ft/s and the unit Reynolds number for this speed of 550,000. This unit Reynolds number allows comparison between the models since the solid disk has a larger chord length than the other tested models.

When examining the aerodynamic data it is important to note that a positive elevator deflection relates to an elevator trailing edge deflected in the downward direction.

5.2.1 Aerodynamic characteristics without transition strip

Figures 5.1 through Figures 5.4 show the lift coefficient, drag coefficient, drag polar and pitching moment coefficient of the case when the flap deflection (δ_F) is zero but the elevator deflection (δ_e) varies from -20 to 20 degrees in 10 degree increments. Cases for δ_F = 10 and 20 degrees and with varying elevator can be found in Appendix A.

The tables presented in this chapter are categorized as follows: Table 5.1a-c is a comparison of the lift coefficients, Table 5.2a-c is the comparison of the drag coefficients and Table 5.3a-c is a comparison of the drag polar. These tables show values for different flap settings while the elevator deflection was varied between -20 and 20 degrees.

Figure 5.1 shows that with elevator deflection angles of 10 and 20 degrees, there is not much change in the C_L curve while the other elevator deflections show a relatively constant difference. This trend was also observed for the other flap deflections as well.

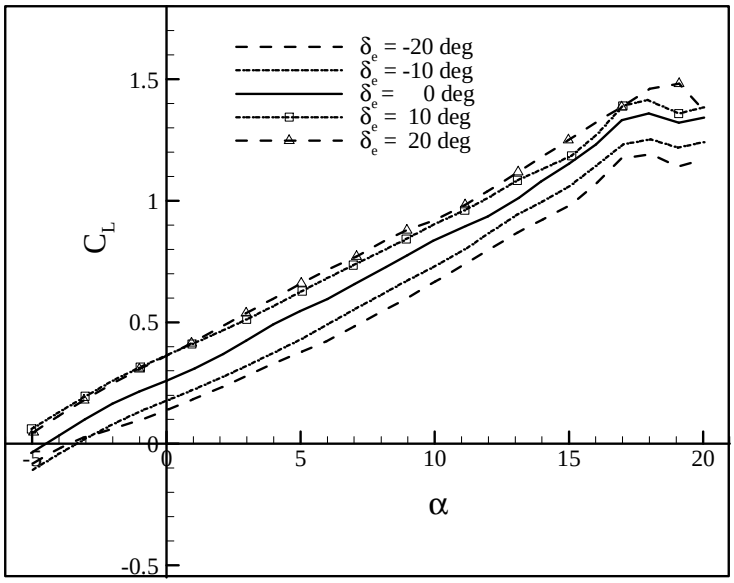

Figure 5.1 Lift coefficient for $\delta_F = 0$ deg

When comparing Tables 5.1a-c it can be seen that with increasing flap deflection $\alpha_{L=0}$ is increased. The lift curve slope remains relatively constant through the range of angles of attack. When increasing the flap setting from 0 to 10 degrees there is not much change in C_{Lmax}, but there is a noticeable difference from 10 to 20 degree flap setting as seen in the Tables 5.1a-c. There is also a noticeable difference in the angle of attack at zero lift.

Table 5.1a Lift coefficient ($\delta_F = 0$ deg)

δe	$\alpha_{L=0}$	a	C_{Lmax}	α stall
-20	-1.5	0.0578	1.25	18
-10	-2	0.0578	1.29	18
0	-3.5	0.0578	1.32	18
10	-4.5	0.0578	1.41	19
20	-4.5	0.0578	---	---

Table 5.1b Lift coefficients (δ_F = 10 deg)

δe	$\alpha_{L=0}$	a	C_{Lmax}	α stall
-20	-2.25	0.0567	1.25	18
-10	-2.75	0.0567	1.28	18
0	-4.0	0.0567	1.39	18
10	-5.25	0.0567	1.44	19
20	-5.25	0.0567	---	---

Table 5.1c Lift coefficients (δ_F = 20 deg)

δe	$\alpha_{L=0}$	a	C_{Lmax}	α stall
-20	-2.0	0.0574	1.32	19
-10	-2.5	0.0574	1.36	19
0	-4.75	0.0574	1.41	19
10	-5.75	0.0574	1.49	19
20	-5.75	0.0574	1.52	19

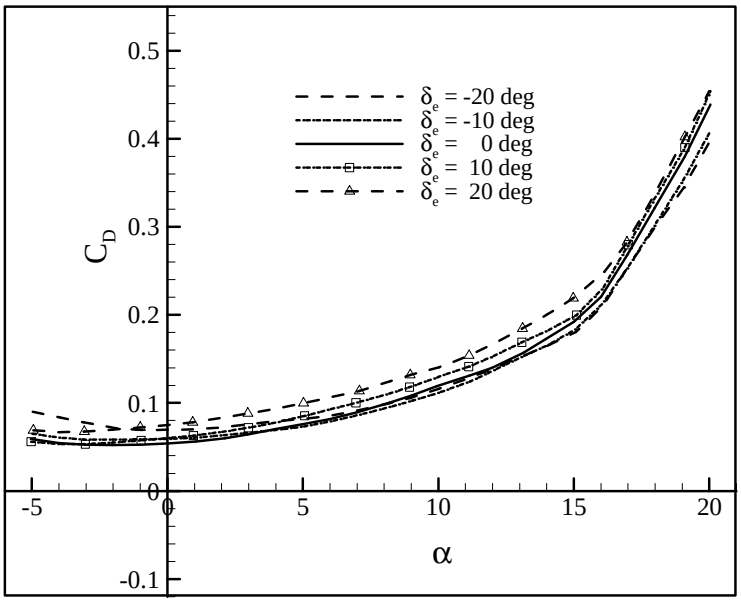

Figure 5.2 Drag coefficient for δ_F=0 deg

As the elevator deflection is changed from 0 deg to 20 deg there is an increase in drag through the angle of attack range, where there is not much change from a 0 to -20

degree deflection as shown in Figure 5.2. When comparing Tables 5.2a-c, as the flap deflection increases the angle of attack for minimum drag decreases. As expected, there is an increase in C_{Dmin} as the flap deflection is increased. This can also be seen in Tables 5.2a-c.

Table 5.2a Drag coefficient ($\delta_F = 0$ deg)

δe	α_{CDmin}	C_{Dmin}
-20	0.25	0.06
-10	0	0.047
0	-2.0	0.04
10	-2.5	0.041
20	-2.0	0.054

Table 5.2b Drag coefficients ($\delta_F = 10$ deg)

δe	α_{CDmin}	C_{Dmin}
-20	-0.5	0.06
-10	-1.0	0.048
0	-1.5	0.043
10	-3.0	0.044
20	-3.0	0.056

Table 5.2c Drag coefficients ($\delta_F = 20$ deg)

δe	α_{CDmin}	C_{Dmin}
-20	-1.0	0.068
-10	-3.0	0.055
0	-3.0	0.049
10	-4.0	0.049
20	-4.0	0.061

The drag polar is another way to examine aerodynamic performance of the aircraft. A combination of the lift and drag coefficients is presented in Figure 5.3. From this plot,

parameters can be examined such as C_{Dmin}, C_{D0} (at C_L=0), as well as lift to drag ratios can be examined.

Drag polar plots allow easy interpretation to find the L/D_{max} of the aircraft. This is a direct measurement of the aerodynamic efficiency of a given airplane. It plays a role in dictating maximum velocity, maximum rate of climb as well as range and endurance [3]. Tables 5.3a-c show the L/D_{max} and the associated angles of attack. The largest L/D ratio for all flap deflection cases is 8.28 and occurs at δ_e of 10 degrees with a corresponding α = 6 deg. This means the aircraft can lift 8.28 lb of weight at a cost of 1 lb of drag. With an increasing in flap deflection the L/D_{max} values decrease. Overall, for any flap deflection range and endurance would be maximized with an elevator trimmed for δ = 10 deg.

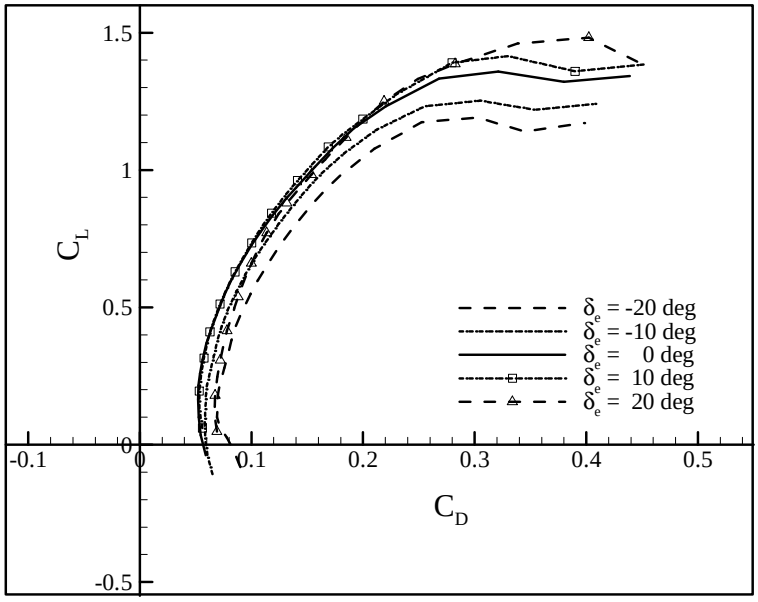

Figure 5.3 Drag polar for δ_F = 0 deg

Table 5.3a Drag polar (δ_F = 0 deg)

δ_e	α of L/D_{max}	L/D_{max}
-20	12	6.40
-10	10	7.40
0	7	8.15
10	6	8.28
20	6	7.62

Table 5.3b Drag polar (δ_F = 10 deg)

δe	α of L/D_{max}	L/D_{max}
-20	11	6.19
-10	9	7.22
0	7	8.09
10	6	8.07
20	7	7.52

Table 5.3c Drag polar (δ_F = 20 deg)

δe	α of L/D_{max}	L/D_{max}
-20	10	5.90
-10	8	6.81
0	7	7.26
10	6	7.60
20	6	7.1

Another important longitudinal analysis tool when examining the performance of an aircraft is its stability. It is critical for the aircraft to be stable through the angle of attack range. In order for the aircraft to be stable, the pitching moment when plotted against α must have a negative slope. By examining Figure 5.4, it is clear that negative elevator

deflections produce an unstable aircraft up to around 5 degrees AoA where the slope of the curve changes and the aircraft become stable. With positive and no elevator deflection is can be seen that the aircraft remains neutrally stable up to 5 degrees angle of attack and then becomes more stable up to stall.

It is important to note that the stability of the airplane is strongly influenced by the c.g. position. While the above data show the Geobat is unstable at the measured c.g. location of the model, it can be made stable by moving the c.g. location forward. An analysis of the neutral point of the aircraft is discussed in Chapter 6.

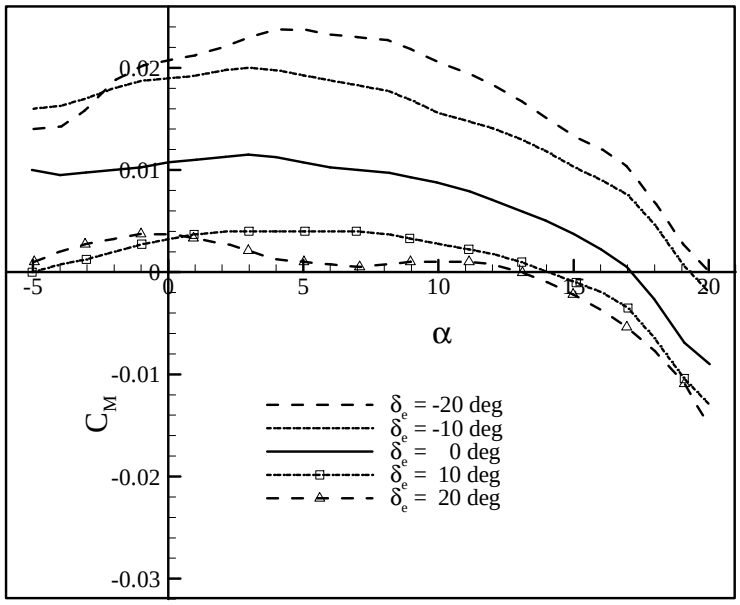

Figure 5.4 Pitching moment coefficient for δ_F = 0 deg

5.2.2 Comparison with and without transition strip

For this series of tests, the Geobat was tested at angles of attack and all possible flap and elevator deflections with and with out the transition strip. Figure 5.5 through Figure

5.7 are coefficient plots with a fixed flap setting and varying elevator while Figure 5.8 through Figure 5.10 are plots with a varying flap and fixed elevator setting. For simplification purposes transition strip will be denoted by TS.

Figure 5.5 reveals that there is a slight change in C_L between the two cases. The flow cases without the TS have a slightly higher lift coefficient through the entire range of angles of attack up to stall. Near the stall region and with the TS, the elevator deflections of -20 and 0 degrees show larger C_{Lmax} and delay stall in comparison to without the TS. For example, with no TS, the case for $\delta_F = 0$ and $\delta_e = 0$ has a C_{Lmax} of 1.30 and stalls at 18 degree α, where the case with the TS has a C_{Lmax} of 1.42 stalling at 19 degree α, yielding an 8% difference.

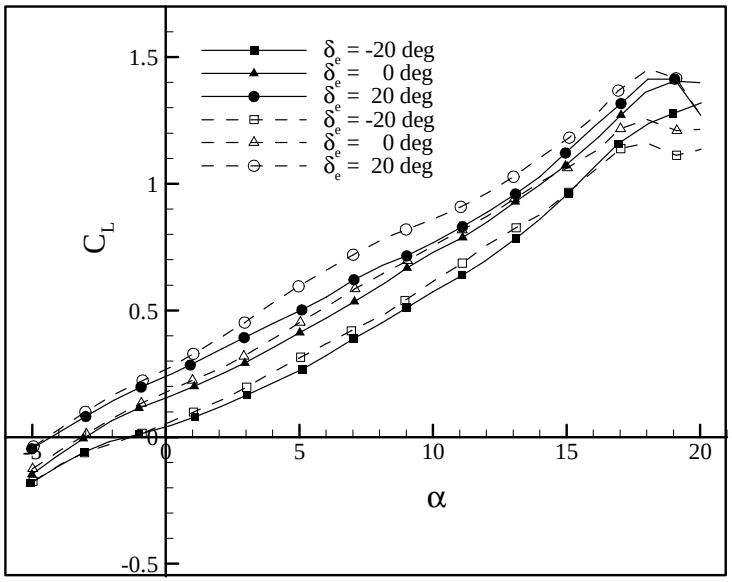

Figure 5.5 With and without TS comparison of lift coefficient for $\delta_F = 0$ deg; solid symbols- with TS, open symbols- without TS

Figure 5.6 represents the drag polar for the cases with and without the TS. As shown in the previous figure, there is a noticeable change in the maximum lift coefficient.

Changes in the drag coefficients for both cases can be considered negligible. For the entire range of angles tested, when comparing the difference in both cases, the drag coefficient has a maximum variance of 3%.

Figure 5.7 shows the pitching moment coefficient for both cases. The ΔC_M without the TS case is slightly higher than the one with the TS. For both cases, this figure still shows a neutrally stable aircraft up to around 5 degrees α while increasing in stability thereafter.

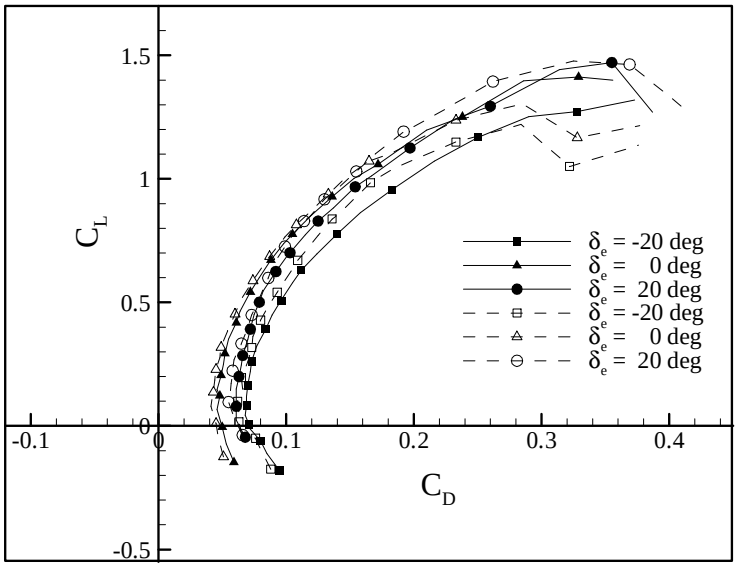

Figure 5.6 With and without TS comparison of drag polar for $\delta_F = 0$ deg; solid symbols- with TS, open symbols- without TS

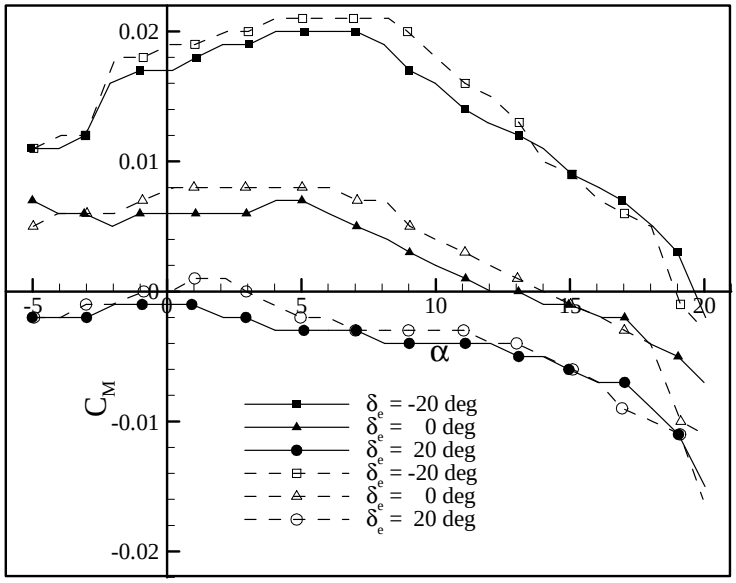

Figure 5.7 With and without TS comparison for pitching moment coefficient for $\delta_F = 0$; solid symbols- with TS, open symbols- without TS

There are some noticeable differences when setting $\delta_e = 0$ and varying δ_F. The stall region presented in Figure 5.8 closely resembles Figure 5.5. The presence of the transition strip prevents stall and leads to a higher C_{Lmax}. A noticeable difference between the two lift curves is the effects of elevator and flap deflections. The change in lift coefficient is smaller when varying the flap setting compared to varying the elevator setting.

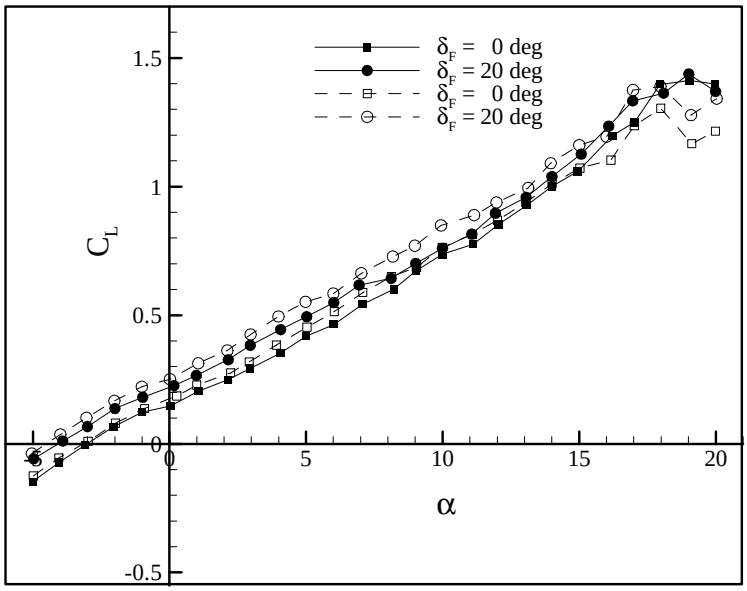

Figure 5.8 With and without TS comparison for lift coefficient for $\delta_e = 0$ deg; solid symbols- with TS, open symbols- without TS

There is not much change when comparing Figure 5.6 and Figure 5.9. The difference in maximum lift to drag ratio as well as minimum drag coefficient can be considered negligible. There is a noticeable difference when comparing the pitching moment coefficients of Figure 5.7 and Figure 5.10. By varying the flap setting and keeping the elevator constant, the aircraft possesses more stable characteristics through the angle of attack range. More stable characteristics can be seen in Figure 5.10 in the lower angle of attack range with the addition of the transition strip.

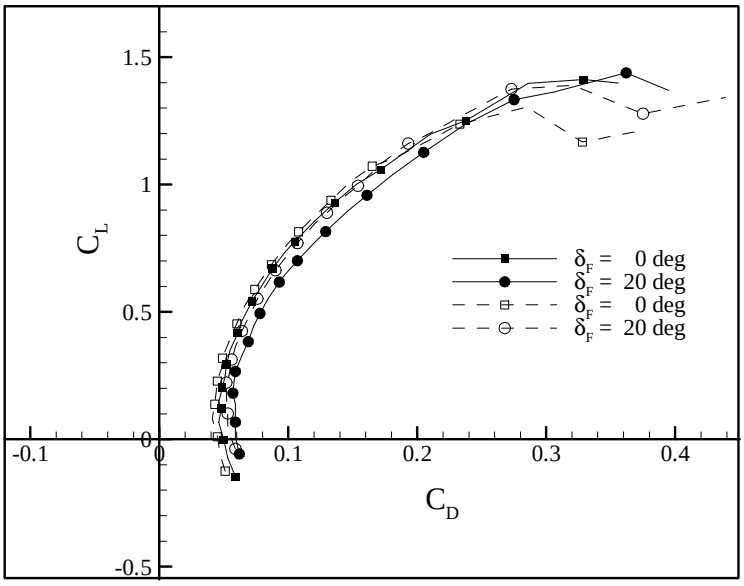

Figure 5.9 With and without TS comparison for drag polar for δ_e = 0 deg;
solid symbols- with TS, open symbols- without TS

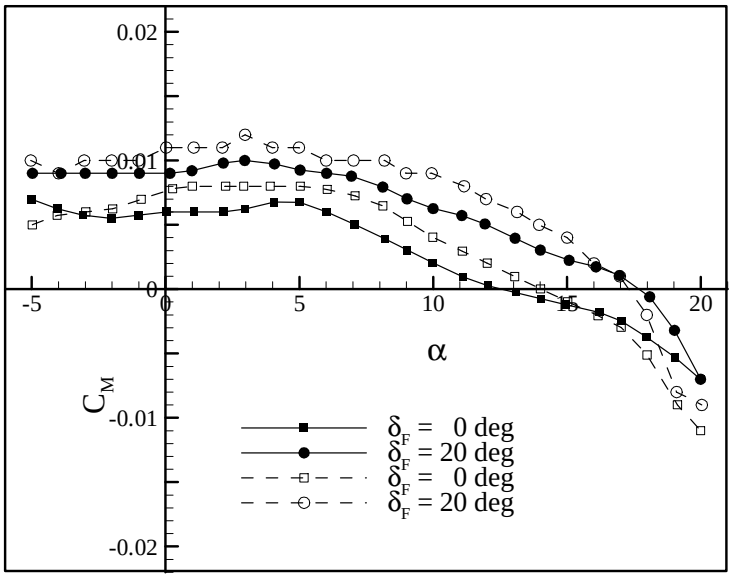

Figure 5.10 With and without TS comparison for pitching moment coefficient for δ_e = 0 deg;
solid symbols- with TS, open symbols- without TS

It is concluded from Figures 5.5 to 5.10 that the addition of the transition strip did not affect the flow properties of the Geobat except near the stall region. This means that the flow over the model without the transition strip is fully turbulent. The cause of the turbulent flow without the transition strip is described with flow visualization seen in Section 5.5.

5.3 Geobat and flat disk comparison

Due to nonlinear lift through the range of α, two different lift curve slopes were calculated for each model to see the difference in low and high α regions. One slope between the angles of -5 and 10 degrees, ([a] in Table 5.1) and another slope between the angles of 10 degrees and stall ([b] in Table 5.1). This was done by linear regression. By observing Figure 5.11, the difference between the lift curve slope of the Geobat (both with and without transition strip) and the similarly contoured cutout disk can clearly be noticed. The difference is attributed to the larger regions of separated flow due to sharper leading edges of the cutout disk that could not reattach adequately at higher angles of attack. This trend continues as the lift coefficient levels and becomes insensitive to changes in angle of attack. It is evident that the solid disk does not stall in the range of angles tested.

To compare to the theoretical lift slope for an aspect ratio of 2.53, Equation 1.2 from Chapter 1 was used and plotted in Figure 5.11. A value of e = 0.90 was chosen for calculation. A value of a_0 = 0.106 per degree was found from linear regression using NACA 23012 airfoil data for an infinite wing [18], the same series found on the Geobat. The theoretical lift slope for an aspect ratio of 2.53 then becomes, a = 0.0573 per degree.

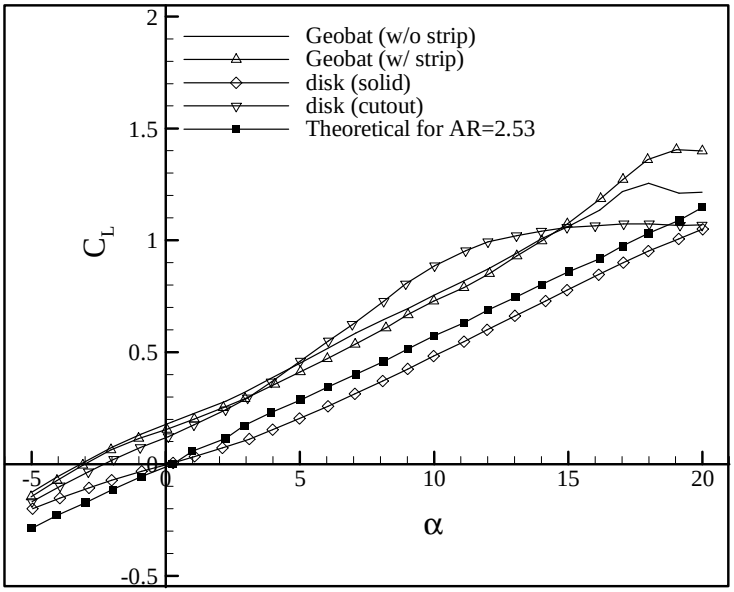

Figure 5.11 Lift curve- Geobat and disk comparison

Table 5.4 summarizes lift coefficient related parameters for each model tested and shows that the Geobat model without a transition strip followed the same lift curve slope as that of the Geobat model with the transition strip up to 10 degrees angle of attack. From this point onward, the Geobat model with the transition strip encountered a larger lift slope of 0.068, a 14% increase and a larger C_{Lmax} = 1.42, a 7% increase. The cutout disk on the other hand exhibited a larger lift slope until it reached 10 degrees α where it fell to 0.025 per degree and reached a C_{Lmax} = 1.08, a 24% decrease compared to the Geobat with transition strip.

Following Prandtl's lifting line theory; it can be seen from Table 5.4 that the lift slopes closely agree to the theoretical value with the Geobat having almost identical values. This shows that the Geobat has the desired lift slope for that given aspect ratio.

Table 5.4 Lift characteristics- Geobat and disk comparison

	Geobat without strip	Geobat with strip	Cutout Disc	Solid Disc
$\alpha_{L=0}$	-3.25	-3	-2.25	0.25
a [a]	0.058	0.058	0.066	0.043
a [b]	0.058	0.068	0.025	0.047
C_{Lmax}	1.32	1.42	1.08	1.05
Stall α	19	19	17-20	N/A
$C_{L\alpha=0}$	0.175	0.146	0.108	0

Table 5.5 summarizes the drag related parameters presented in the drag polar of Figure 5.13. The drag polars for both Geobat models are very much similar and differ only in the stall characteristics. The solid disk had the lowest drag coefficient C_{Dmin} = 0.025. The cutout disk results were unlike any of the Geobat models. Both the Geobat models yielded L/D_{max} of 8.15 and 7.65, respectively and are larger than that of the cutout disk and double that of the solid disk.

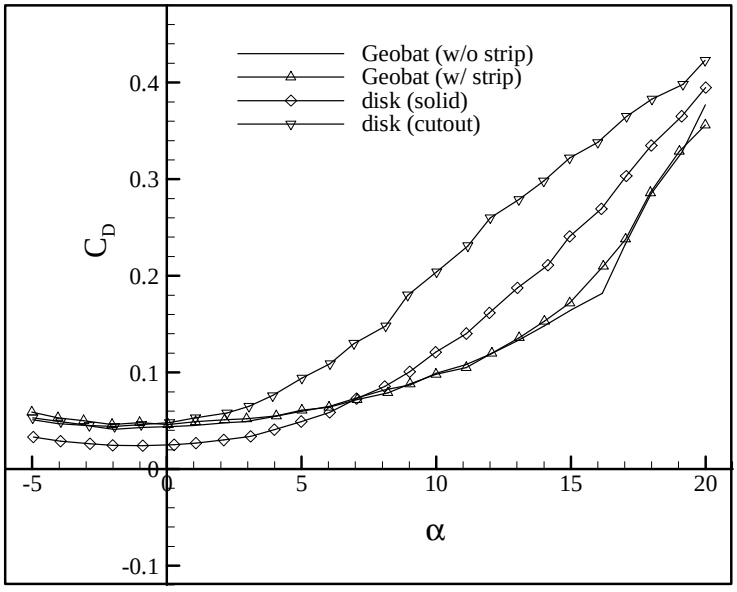

Figure 5.12 Drag Curve- Geobat and disk comparison

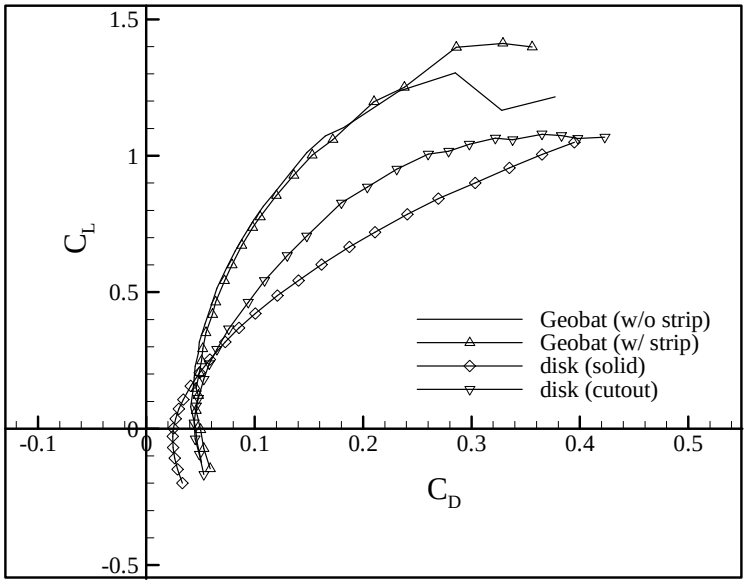

Figure 5.13 Drag Polar- Geobat and disk comparison

Table 5.5 Drag characteristics- Geobat and disk comparison

	Geobat without strip	Geobat with strip	Cutout Disc	Solid Disc
C_{D0}	0.045	0.05	0.045	0.025
$C_{D0}\alpha$	-2	-2	-1	0
L/D_{max}	8.15	7.65	5	4.35
Max α	7	9	6	7

Figure 5.14 shows the trends for the pitching moment of the models. All models other than the solid disks show relatively neutral to stable [17] trends for the range of angles of attacks tested. The pitching moment coefficient for the Geobat models and the cutout disk remain unchanged up to 9 degrees α and followed by a linear decrease between 9 degrees and 20 degrees α. This pattern is similar to the pitching moment characteristics of a NACA 23012 infinite airfoil [18]. Due to the differences in mounting positions the solid disk shows an unstable characteristic up to the 11 degree mark and then begins to stabilize.

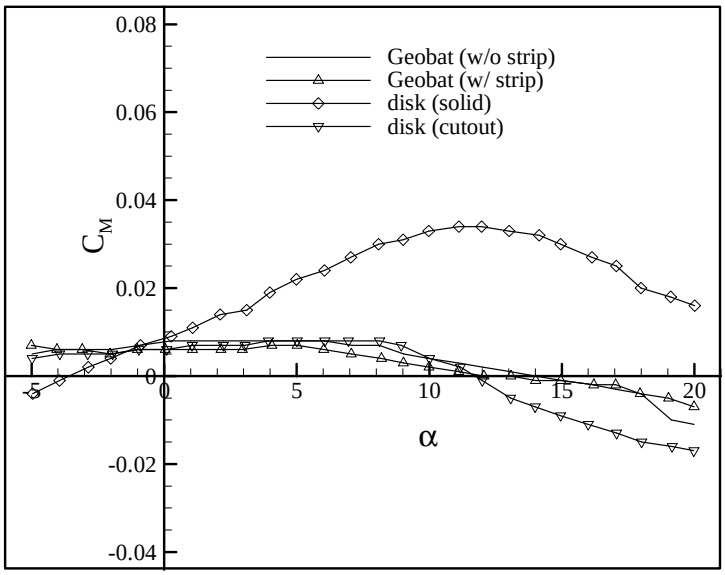

Figure 5.14 Pitching moment- Geobat and disk comparison

5.4 Geobat and Cessna 172 comparison

The figures presented in this section relate to a fixed δ_F = 0 degrees and a varying δ_e = -20, 0 and 20 degrees. For comparison, plots comparing varying flap settings and fixed elevator are located in Appendix A.

Figure 5.15 shows a comparison of the lift coefficients between the Geobat and Cessna 172 model. It was noticed that the lift slope for the Cessna 172 was larger than that of the Geobat but the stall angle of 14 degrees was lower compared to 19 degrees of the Geobat. As explained in Chapter 1, the trends of these two models agree with varying aspect ratio relationships. The Geobat has a smaller lift curve slope while low aspect ratio characteristics allow the aircraft to have a larger stall angle. Due to the small effect that induced drag has at lower angles of attack, $\alpha_{L=0}$ should be closely related for a given airfoil independent of the aspect ratio [1]. Although the airfoil sections are different for

both the Geobat and Cessna 172, it can be seen in Figure 5.15 that the angle of attack where the lift is equal to zero are very similar for both models. For comparison, a Clark Y airfoil has an $\alpha_{L=0}$ = -2 degrees where a NACA 23012 has an $\alpha_{L=0}$ = -2 degrees.

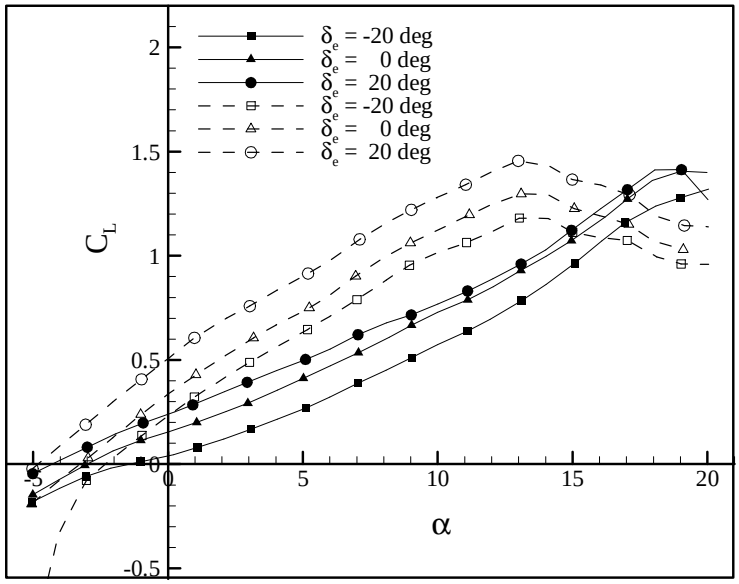

Figure 5.15 Lift curve- Geobat and Cessna comparison for δ_F = 0 deg;
solid symbols- Geobat, open symbols- Cessna 172

Figure 5.16 shows the comparison of drag for both models with a fixed flap and varying elevator setting. Drag trends for both models are relatively equal with higher drag for the Cessna after stall.

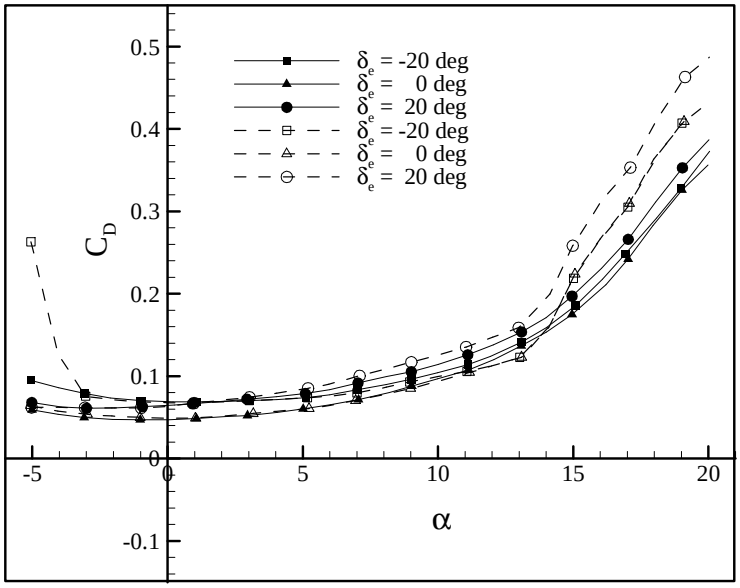

Figure 5.16 Drag curve- Geobat and Cessna comparison for $\delta_F = 0$ deg; solid symbols- Geobat, open symbols- Cessna 172

Plotting C_L vs. C_D, shown in Figure 5.17, reveals a higher maximum lift to drag ratio for the Cessna 172, $L/D_{max} = 11$, in comparison to the Geobat, $L/D_{max} = 7.5$. This difference in L/D_{max} agrees with the theory behind the difference in the aspect ratios. It is also noticed that as the lift coefficient increases for the Geobat, the drag coefficient increases much faster than that of the Cessna 172, again contributing to a smaller lift to drag ratio. Relatively the same values are present in both models for C_{Dmin} and α_{CDmin} for each setting.

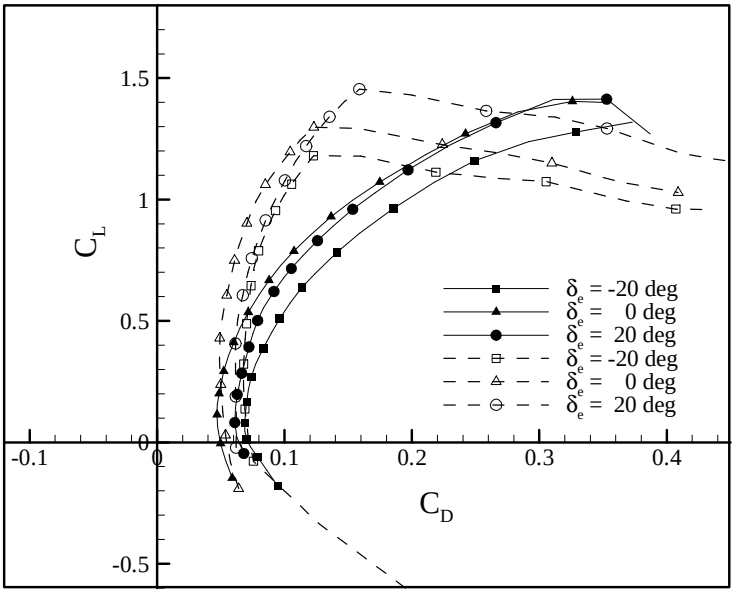

Figure 5.17 Drag polar- Geobat and Cessna comparison for δ_F = 0 deg;
solid symbols- Geobat, open symbols- Cessna 172

There is a noticeable difference in the pitching moment coefficient plot between the two models, presented in Figure 5.18. The Cessna 172 shows static stability through the entire angle of attack range compared to the mostly neutrally stable trend of the Geobat. The pitching moment coefficient slope for the Geobat model remains neutrally stable up to 9 degrees α and followed by a linear decrease in slope between 9 degrees and 20 degrees α. This pattern is similar to the pitching moment characteristics of a NACA 23012 series airfoil [18]. For both models, an elevator deflection of 20 degrees demonstrates a positive stiffness (shown by a negative pitching slope) but they are both unbalanced (shown by having a negative value of C_{M0}). C_{M0} must be positive along with a negative pitching slope if the airplane is to meet the condition for stable equilibrium [17].

Figure 5.19 shows a large difference for change in flap setting when compared to Figure 5.18. C_{M0} for both models have shifted as well as the ΔC_M between the flap

settings of the Cessna 172. There is not as much as a variance in the pitching moment when changing the flap settings while maintaining a constant elevator deflection, which is expected.

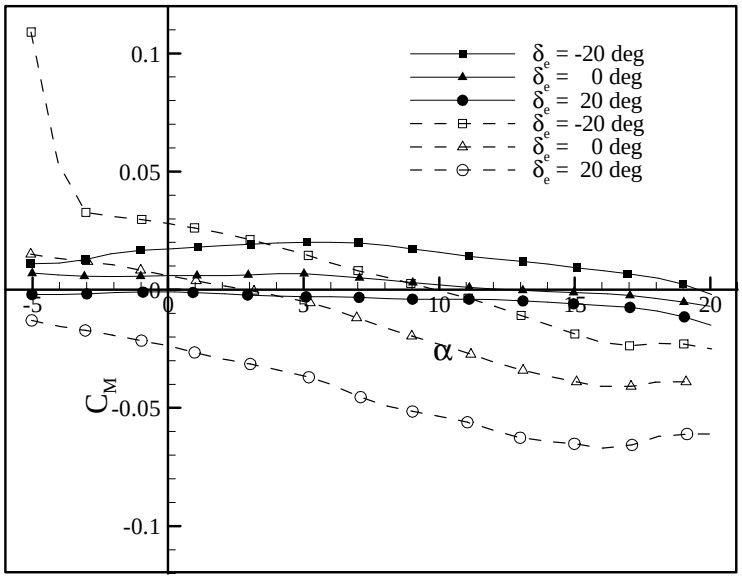

Figure 5.18 Pitching moment curve- Geobat and Cessna comparison for $\delta_F = 0$ deg; solid symbols- Geobat, open symbols- Cessna 172

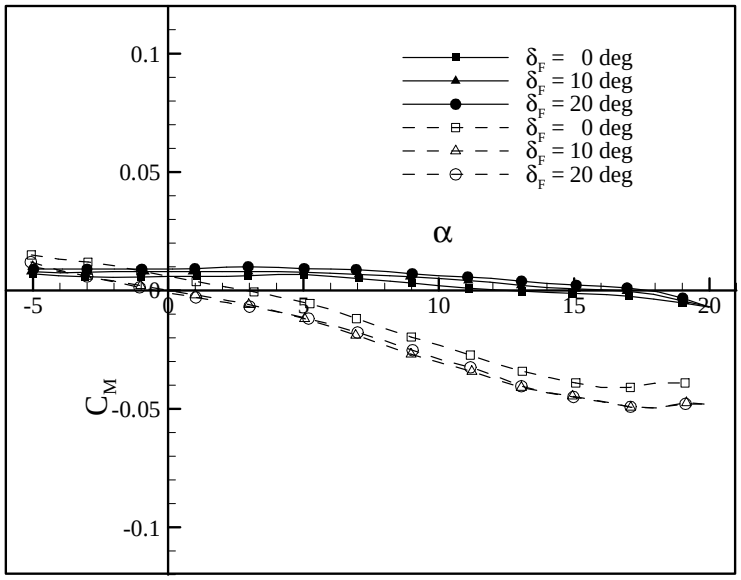

Figure 5.19 Pitching moment curve- Geobat and Cessna comparison for $\delta_e = 0$ deg; solid symbols- Geobat, open symbols- Cessna 172

5.5 Flow Visualization

As stated earlier, flow visualization tests were conducted at 100 ft/s. The flat disk models were tested at 0, 5, and 10 degrees α, while results from the Geobat are shown at -5, 0, 5, 10, 15 and 20 degrees α. The visualization fluid was brushed over the top surface of the model.

5.5.1 Flat disks

Presented in Figure 5.20 and Figure 5.21 are the flow visualization results of the upper surfaces of the solid disk and cutout disk positioned at α = 0 deg. There is a small leading edge crescent shaped separation bubble that was formed on both models. Turbulent reattachment occurs directly behind this separation bubble. Boundary layer growth over the model's surface causes less viscous shear in the streamwise direction as the flow is moved downstream. This can be seen by the dye collection over the middle and rear of the models. This is more predominant for the solid disk model.

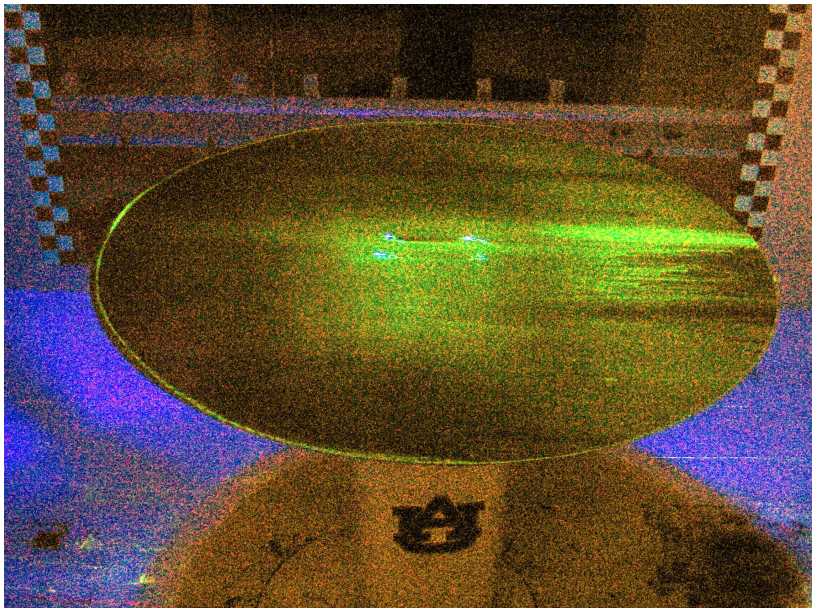

Figure 5.20 Solid disk flow visualization at α = 0 deg

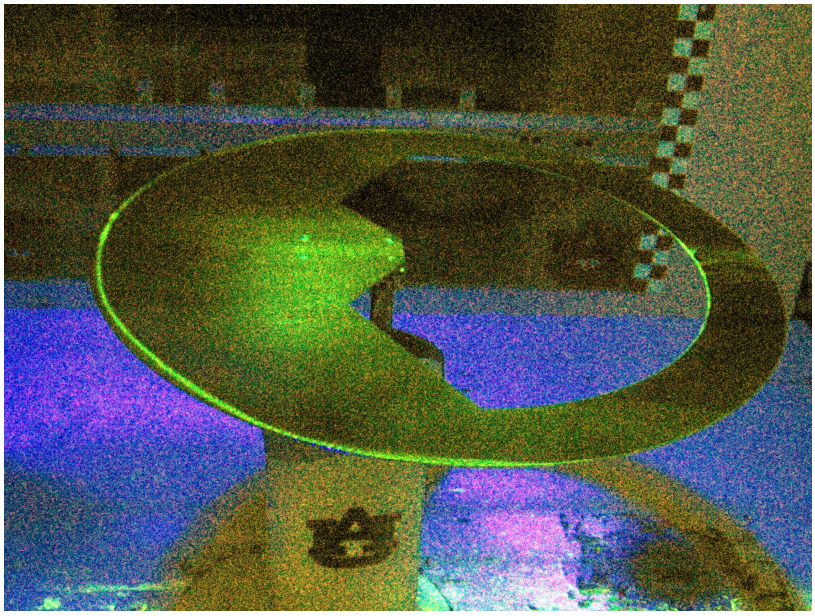

Figure 5.21 Cutout disk flow visualization at α = 0 deg

By examining Figures 5.22 and 5.23 at α = 5 degrees, it can be seen that there is a crescent-shaped, short boundary layer separation bubble that is marked by the accumulation of fluorescent dye and results in turbulent reattachment and thus scraping of downstream dye. It was noted that in the case of the solid disk, the reattached flow remained attached without any secondary separation as the boundary layer thickened. The cutout disk also showed attached flow downstream of the separation bubble.

An interesting feature of the circular attachment line was the double cellular structure of the separation bubble near the leading edge as well as a more jagged structure located at the outer edges of the disks.

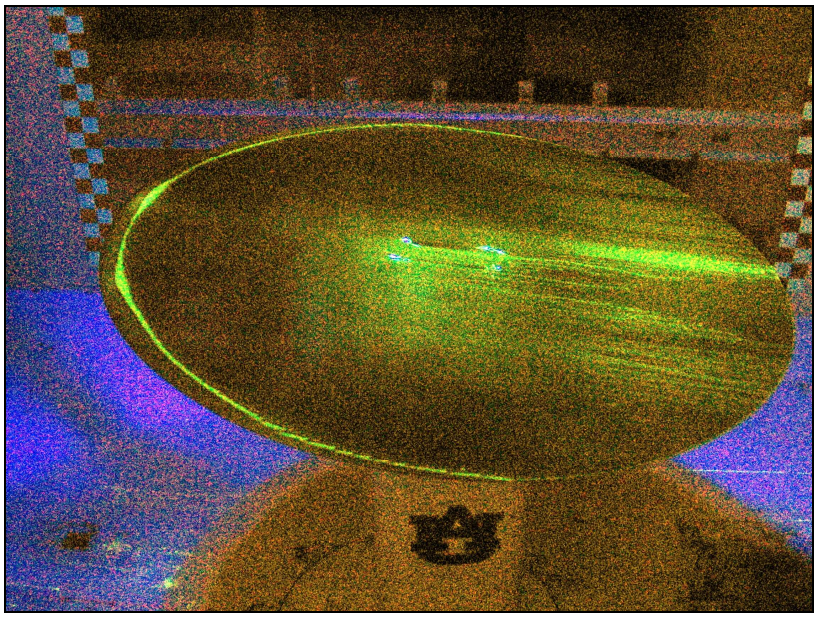

Figure 5.22 Solid disk flow visualization at α = 5 deg

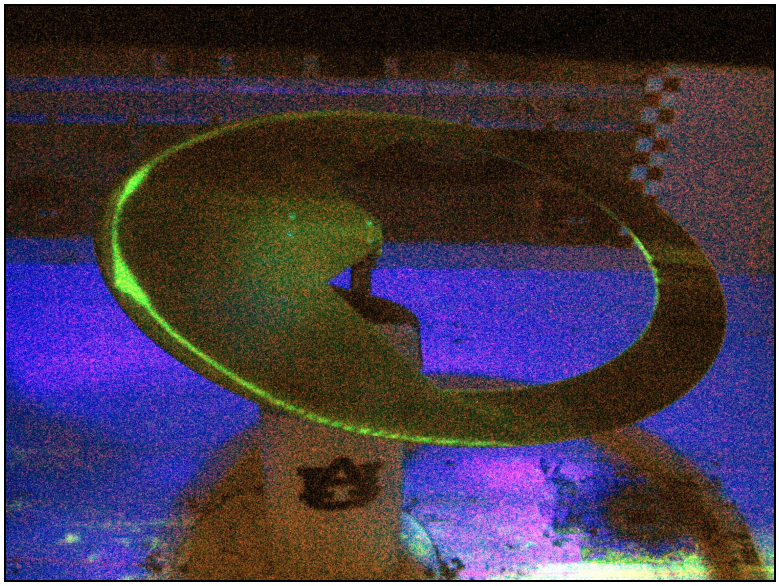

Figure 5.23 Cutout disk flow visualization at α = 5 deg

As the angle of attack of the models is increased to α = 10 degrees, as shown in Figure 5.24 and 5.25, the same separation bubble occurs but is much more jagged and is moved further back from the leading edge. This increased distance of separation causes

recirculation of the flow back towards the leading edge as noticed by the lines of fluid in front of the separation bubble. Although this reflects chaotic motion of the fluid, there is still reattachment after the separation bubble as seen in the lift curve of Figure 5.11. This holds true for increased angles of attack.

It was also noticed that the separation bubble near the outer edge of the model has increased in length. Downwash on the outer surface could cause this movement as the strength of the tip vortices has increased.

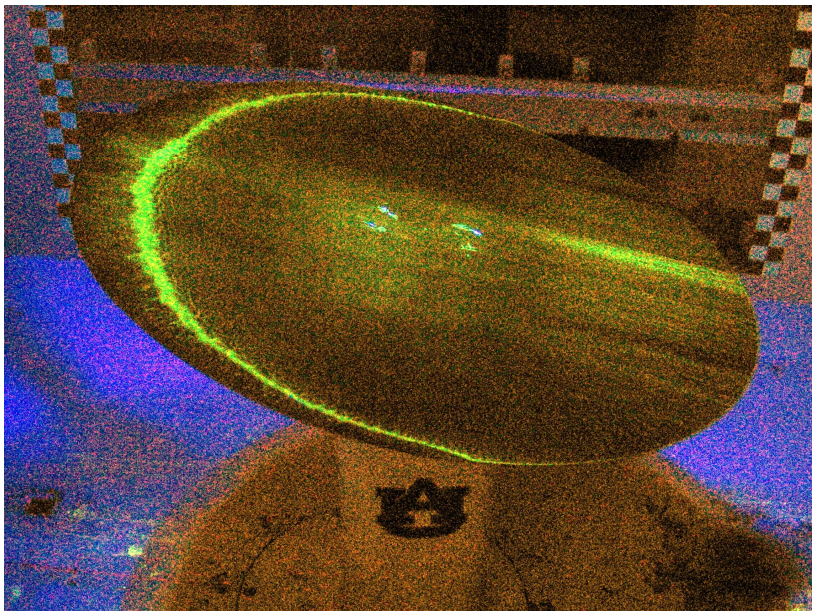

Figure 5.24 Solid disk flow visualization at α = 10 deg

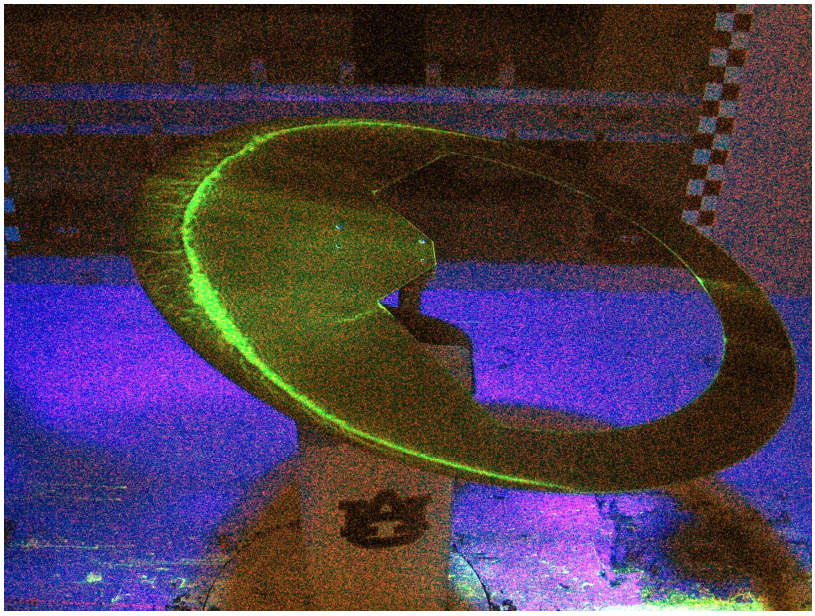

Figure 5.25 Cutout disk flow visualization at α = 10 deg

5.5.2 Geobat

Flow visualization of the Geobat aircraft at several different angles of attack are presented in the following figures. A continuation of these figures can be found in Appendix B where different view points of the model are shown.

Figure 5.26 reveals laminar attached flow with no separation bubble located on the model. There is a large separation region located on the trailing edge of the elevator as well as separation on the cockpit. This detached flow is also found for α = 0 deg shown in Figure 5.27 with even more predominant separation over the cockpit. This separation found on the elevator as well as complete laminar flow leading wing could be the reason for the neutrally stability found in the pitching moment plots.

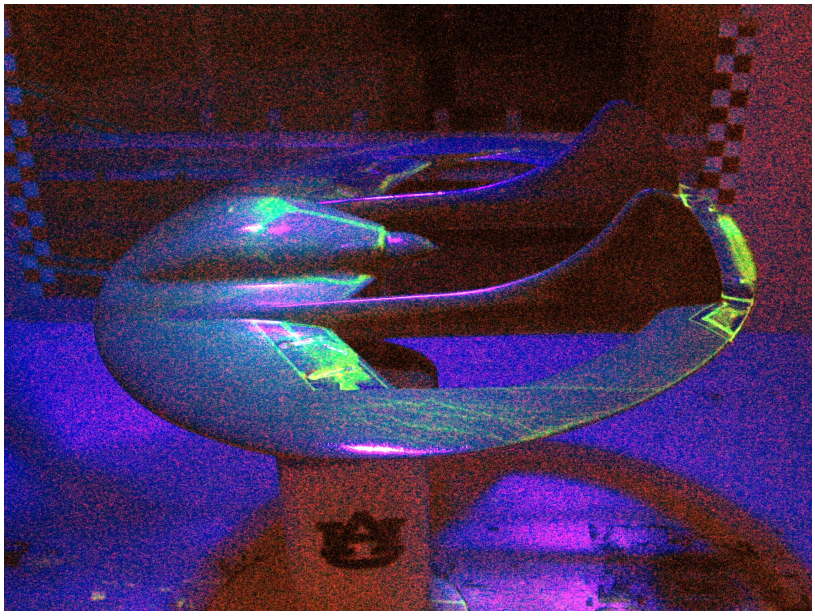

Figure 5.26 Geobat flow visualization at α = -5 deg

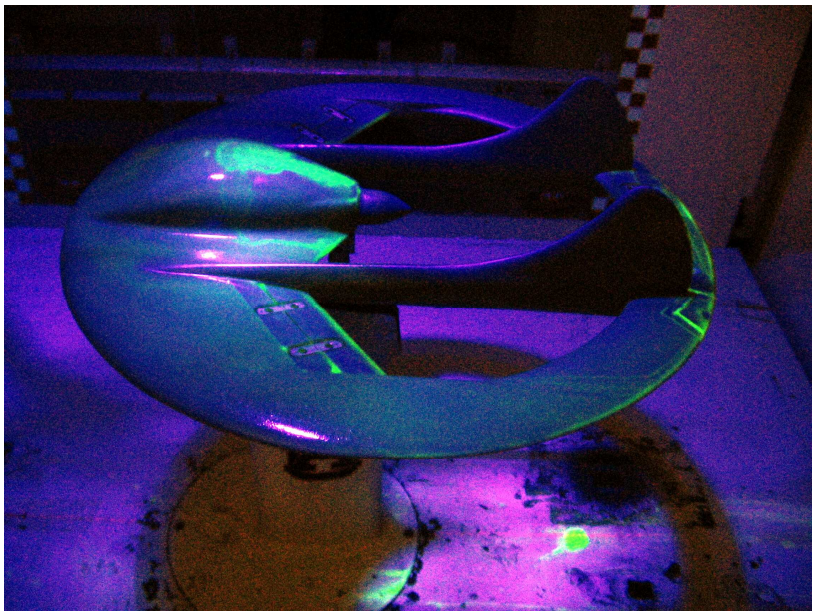

Figure 5.27 Geobat flow visualization at α = 0 deg

As the angle of attack is increased to 5 degrees there is a noticeable change in the structure of the flow with the addition of the separation bubble on the leading edge of the

airfoil. Figure 5.28 shows this trend but still yields the same separation on the trailing edges of the control surfaces as well as separation on the top of the cockpit.

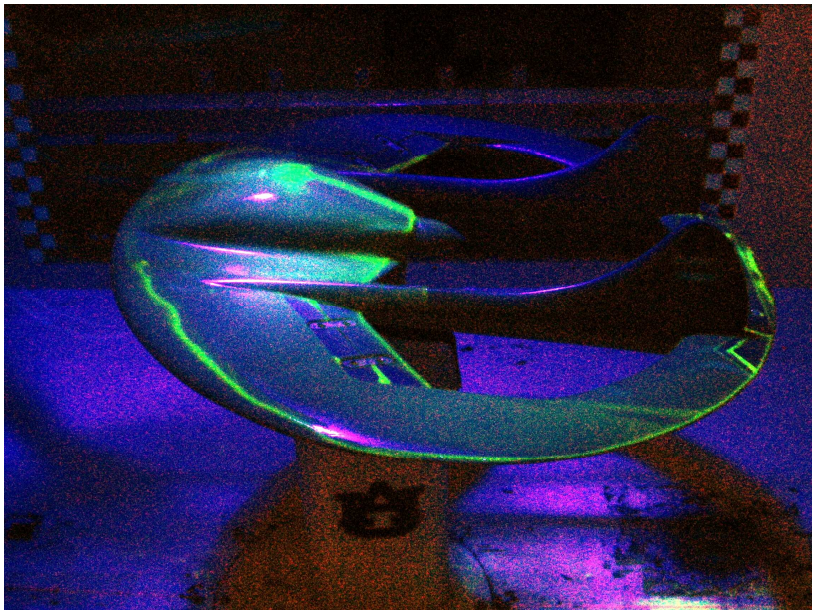

Figure 5.28 Geobat flow visualization at α = 5 deg

As α is increased to 10 degrees, several different flow characteristics are observed. Figure 5.29 shows complete formation of the separation bubble span wise on the airfoil, unlike the previous figure where it was not present near the cockpit region. This may aid in the formation of a second and third separation bubble that can now be seen on the rear half of the cockpit. Existence of a junction vortex was also noticed in the region just ahead of the mounting location of the rudder attachment. This pattern can be seen more prominently at 15 degrees α as shown in Figure 30. Video evidence also revealed an oscillatory behavior in this region. A secondary separation pattern resembling open separation was observed on the top of the cockpit.

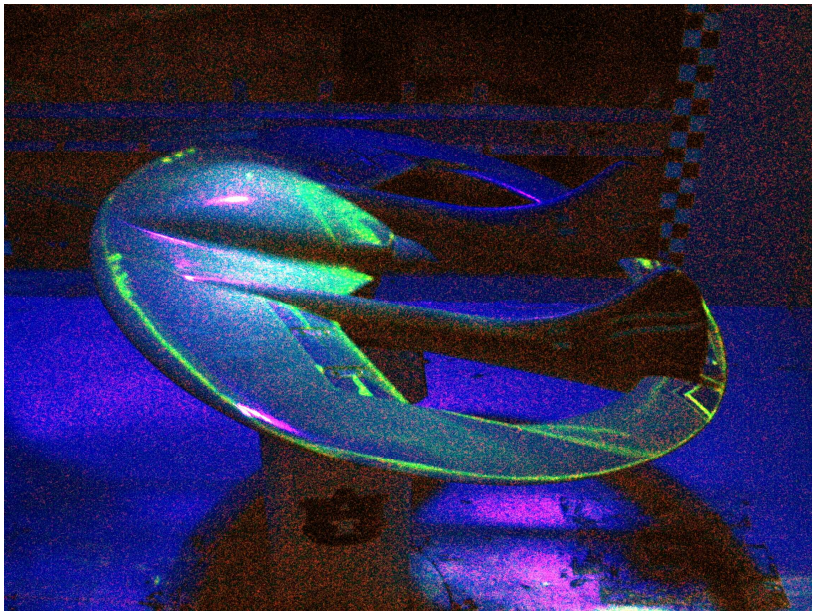

Figure 5.29 Geobat flow visualization at α = 10 deg

One important phenomenon to notice in Figure 5.30 is the wavy structure located near the outer edge of the wing. This is believed to be the formation of the wing tip vortex and the shearing of the vortices on the top surface. Also note that the separation bubble has moved closer to the leading edge of the airfoil which is opposite of the flat plate models. With less interference from the main wing, trailing edge flow detachment of the elevator control surface is less predominant then when at lower angles of attack.

Figure 5.31 shows a complete stall of the aircraft at an angle of attack of 20 degrees. Flow on the upper surface has completely changed direction and is moving towards the front of the aircraft.

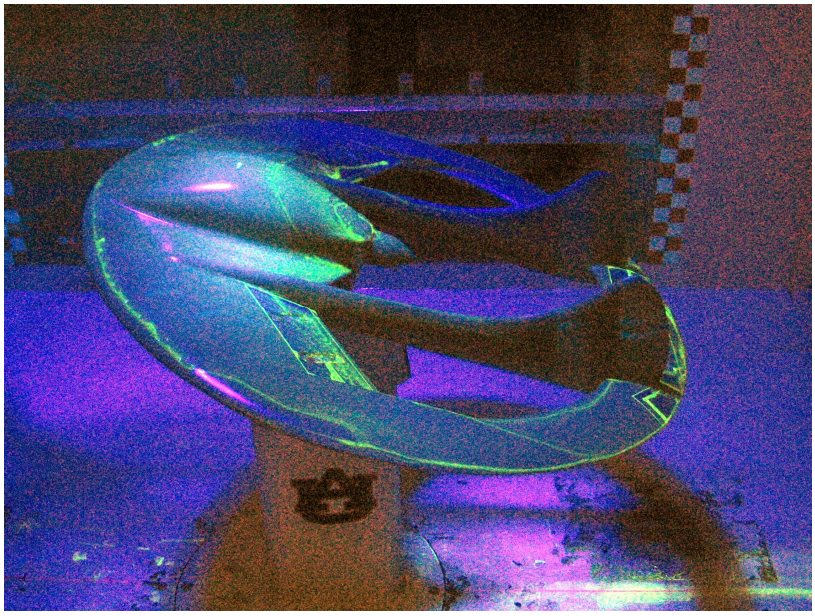

Figure 5.30 Geobat flow visualization at α = 15 deg

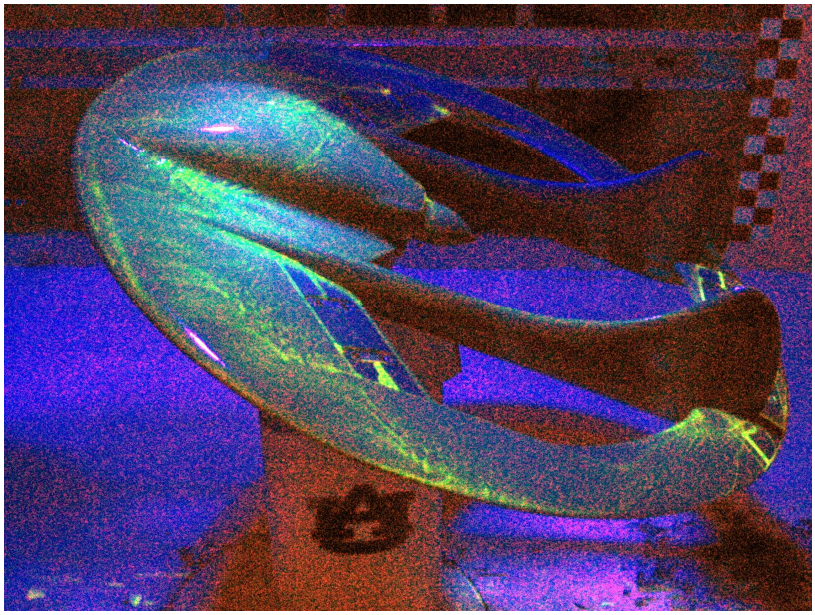

Figure 5.31 Geobat flow visualization at α = 20 deg

6 STABILITY ANALYSIS

6.1 Theory

Tests of the models allow for aerodynamic stability and control analysis using parameters obtained from the data. In this chapter determination of the neutral point and static margin of both the Geobat and Cessna 172 models is presented.

In determining the longitudinal stability of an aircraft, comparison of the aircraft's center of gravity location and neutral point location is of importance. As stated in Chapter 3, only one c.g. location was tested for each of the models and was determined by balancing the aircraft until no pitching was observed. The center of the mount for tests was positioned at this location. For calculation purposes, the Geobat c.g. location was 0.645 ft from the leading edge of the model (35 % of aircraft length) and the Cessna 172 c.g. location was 0.584 ft from the leading edge of the model (32 % of the aircraft length).

There are several ways to determine static stability of a tested aircraft. One way is to determine the lift and pitching moment of the aircraft with the horizontal elevator and stabilizer off, then analyze under the same condition with the elevator and stabilizer on. This allows for downwash and tail geometry to be introduced into the calculations. Tests in this investigation were conducted with the entire aircraft configuration.

For an aircraft to be considered stable, the criterion to be satisfied is that the aircraft must have a negative pitching moment slope ($C_{m\alpha} < 0$) that is, a positive pitch stiffness [17]. From tests, $C_{m\alpha}$ and $C_{L\alpha}$ were used to determine the neutral point location as shown in Equation 6.1, where

$$C_{m\alpha} = C_{L\alpha} (h - h_n) \qquad (6.1)$$

h is the c.g. location and h_n is the location of the neutral point measured from the leading edge.

To satisfy stability, the above equation must prove that $h < h_n$. Equation 6.2 is referred to as the static margin and is the difference between the c.g position and the NP position. From both of these equations it is noticed that the c.g. must be forward of the NP [17]. The farther forward the c.g. is from the neutral point the more statically stable the aircraft is.

$$K_n = (h_n - h) \qquad (6.2)$$

Prior to calculations it is important to understand the effect that the c.g. location has on the C_m curve. Figure 6.1 shows a C_m curve and resulting values of the neutral point and c.g. A negative slope results in the NP being located behind the c.g. of the aircraft resulting in a positive pitching stiffness where a positive slope results in a negative pitching stiffness. The value of $h = h_n$ has a particular interest in that this is the boundary between stable and unstable c.g. locations.

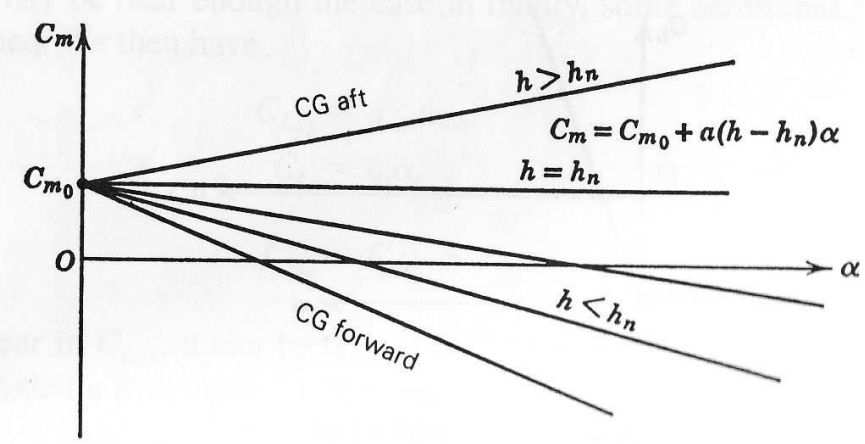

Figure 6.1 Effects of c.g. location on C_m curve [17]

Figure 6.2 shows the relationship between the c.g and NP locations as well as the lift and pitching moment coefficients for zero α. With the c.g. located in front of the NP, any disturbance or pitching up motion will allow the aircraft to pitch back down to equilibrium. An unstable aircraft is one where the c.g. location is behind the NP causing a continuing pitching up motion not allowing the aircraft to return to stable equilibrium.

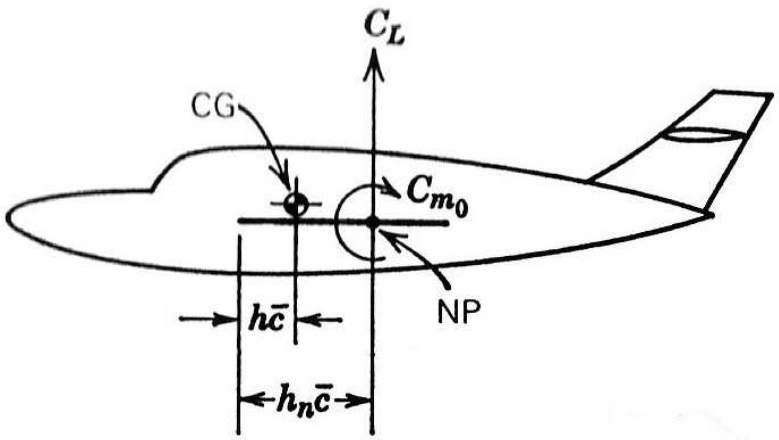

Figure 6.2 Total lift and moment acting on aircraft [17]

6.2 Stability Results

When finding the NP using the pitching moment slope it is assumed that the slope is linear for the entire range of angle of attack. Referring back to Figure 5.18 of the model comparison between the Geobat and Cessna 172 for the pitching moment curve, it is noticed that slope for the Geobat is not linear through the angle of attack range. As stated before, there is a neutral stability trend up to 5 degrees AoA with increasing stability there after. For this reason, calculations of the NP were done from -5 to 5 degrees α and again for 5 to 18 degrees α. The Cessna 172 model possessed a linear trend up to stall and therefore calculations were done from -5 to 13 degrees. Table 6.1 shows values needed for NP calculation of both the Geobat and Cessna 172 model where the $\delta_F = 0$ with varying δ_e.

With the use of Table 6.1 and Equations 1 and 2, the NP and static margin were calculated. These values are displayed in Table 6.2 and compared to Figure 6.1 and Figure 6.2.

Table 6.1 Model values for NP calculation with $\delta_F = 0$ deg

	Geobat			Cessna 172		
	$\delta_e = -20$	$\delta_e = 0$	$\delta_e = 20$	$\delta_e = -20$	$\delta_e = 0$	$\delta_e = 20$
$C_{L\alpha}$	0.0592	0.0622	0.0594	0.0797	0.0821	0.0816
$C_{m\alpha}$ (-5 to 5 AoA)	0.0010	0.00002	-0.0001	-0.0030	-0.0027	-0.0028
$C_{m\alpha}$ (5 to stall AoA)	-0.0012	-0.0008	-0.0004	-0.0030	-0.0027	-0.0028
c.g. location (ft)	0.645	0.645	0.645	0.585	0.585	0.585

Table 6.2 Models NP and static margin for $\delta_F = 0$ deg

	Geobat			Cessna 172		
	$\delta_e = -20$	$\delta_e = 0$	$\delta_e = 20$	$\delta_e = -20$	$\delta_e = 0$	$\delta_e = 20$
(-5 to 5 deg AoA)						
h_n (ft)	0.6281	0.6447	0.6467	0.6226	0.6179	0.6193
K_n (ft)	-0.0169	-0.0003	0.0017	0.0376	0.0329	0.0343
(5 to stall deg AoA)						
h_n (ft)	0.6653	0.6579	0.6517	0.6226	0.6179	0.6193
K_n (ft)	0.0203	0.0129	0.0067	0.0376	0.0329	0.0343

For the lower range of α for the Geobat model it is shown that the NP is in front of the c.g. for δ_e = -20 and 0 deg ($h > h_n$) yielding a positive $C_{m\alpha}$ or negative pitching stiffness. For the same range of α, h_n is almost equal to the c.g. for δ_e = 20 deg ($h = h_n$) showing the boundary between positive and negative pitching stiffness. For α of 5 degrees and higher the Geobat model shows positive stiffness for every δ_e with a maximum K_n = 0.0203 ft at δ_e = 20 deg.

The Cessna 172 is stable through its entire range of α up to stall. The NP is behind the c.g at every δ_e location and has a static margin much larger than the Geobat with a maximum K_n = 0.0376 ft.

The calculations further show that the Geobat model is slightly unstable to neutrally stable below the 5 degrees with increasing stability above 5 degrees. The Cessna 172 model shows that it is much more stable with double the static margin of the Geobat.

The Geobat could have the same static stability as the Cessna 172 model by moving the c.g. location forward. This would increase the static margin, therefore increasing the stability of the aircraft. To have similar longitudinal stability characteristics to the Cessna 172, the Geobat c.g. would need to be moved to a point 0.621 ft aft of the nose versus its current position at 0.645 ft.

7 CONCLUSION

Wind tunnel tests confirmed acceptable aerodynamic characteristics for the Geobat airplane. The Geobat was able to produce lift curves that agreed with the theoretical value from Prandtl's lifting line theory. Both flow cases with and without a transition strip showed drag polars that were similar however the model with the transition strip exhibited a more gradual stall at higher α.

The lift curve shows a higher stall angle for the Geobat with relatively the same C_{Lmax} as the Cessna 172. The lift curve slope of Geobat however was lower than that of Cessna 172 model decreasing the L/D_{max} while drag data revealed a lower minimum drag for the Geobat model and better stall characteristics again following low aspect ratio characteristics.

The pitching moment coefficient for the Geobat indicated neutral stability in the lower α range and higher stability with increasing angle of attack while the Cessna 172 has good stability characteristics through the entire range of angles of attack. This was confirmed by analysis of the NP and static margin of both aircraft.

Comparison of the Geobat to the flat disks showed that the cutout disk had trends similar to the Geobat, but with much higher drag. All models showed trends agreeing with low AR designs.

Flow visualization revealed a crescent shaped laminar separation bubble near the leading edge followed by turbulent reattachment. This visualization confirmed results

that were noted from the aerodynamic data, that the addition of the transition strip did not improve longitudinal characteristics in the lower angles of attack range because the flow was already turbulent in nature. Additional flow structures observed on the Geobat cockpit, control surface trailing edge and pylon mountings may decrease overall performance.

8 RECOMMENDATIONS

This research has allowed for a wide range of applications to be applied to the Geobat model in the search for more promising aerodynamic qualities. By moving the c.g. forward on the model, testing for a more stable aircraft can be done. After viewing the flow visualization it would be a good idea to place more turbulent strips at areas of separation, in particular the cockpit and leading edges of the tail section. This would hopefully keep the flow more attached on the aircraft and may improve the lift as well as the pitching moment of the aircraft.

There are also sections of the aircraft that can be 'fine tuned' in order to improve aerodynamics. The outer edges, or wing tips, seem to be too thick. The aircraft already possesses strong structural integrity due to the design. Unless engines were to be mounted at this region, reduction in thickness may improve its overall characteristics.

Water tunnel tests should also be conducted in depth to further understand the wake of the aircraft. What is the strength of the vortices at the wing tip? How does the flow off of the front of the aircraft affect the horizontal and vertical control surfaces? The novelty of this aircraft has a great potential for improvement and better understanding in low aspect circular planform designs.

REFERENCES

[1] Anderson, J.D., Jr. Aircraft Performance and Design. New York: McGraw-Hill, Inc., 1999.

[2] Anderson, J.D., Jr. Fundamentals of Aerodynamics 3rd ed. New York: McGraw-Hill, Inc., 2001.

[3] Raymer, D.P. Aircraft Design: A Conceptual Approach 3rd ed. Virginia: American Institute of Aeronautics and Astronautics, Inc., 1999.

[4] "Sack AS-6 Luft '46 entry." Sack AS-6. 1997. 8 Jan 2008 <http://www.luft46.com/misc/sackas6.html>.

[5] "VoughtV-173/XF5U-1." Daves war birds. 1999. 3 Jan 2008 <http://www.davveswarbirds.com/usplanes/aircraft/flapjact.html>.

[6] Wainfan, B. "Zimmerman's Flying Flapjack: Designs Ahead of their Time." Flight Journal. (2005): 89-93.

[7] Gudaitis, F. "Charles Zimmerman and his 'Skimmer'." Flight Journal. (2005): 65-71.

[8] Wilson, T. "Americas Nuclear Flying Saucer." Military. 15 January 2008 <http://military.com/Content/MoreContent/?file=PMsaucer>.

[9] Ware, G. "Investigation of the Low-subsonic Aerodynamic Characteristics of a model of a modified Lenticular Reentry Configuration." NASA TM X-756, 1962.

[10] Stilley, G.D. "Aerodynamic Analysis of the Self Sustained Flair." RDTR no 199, Naval Ammunition Depot. Indiana. 1972.

[11] Stilley, G.D., and Carstens, D.L. "Adaptation of Frisbee Flight Principle to Delivery of Special Ordnance." AIAA Paper 72-982. In Proceedings of the 2nd Atmospheric Flight Mechanics Conference, Palo Alto, California. 1972.

[12] Mitchell, T.L. The Aerodynamic Response of Airborne Discs. MS thesis, University of Nevada, Las Vegas, NV. 1999.

[13] Yasuda K. “Fight and Aerodynamic Characteristics of a Flying Disk.” Japanese Soc. Aero. Space Sci. (1999): 16-22.

[14] Potts, J.R., and Crowther, W.J. “Frisbee Aerodynamics.” AIAA Paper 2002-3150. In Proceedings of the 20th AIAA Applied Aerodynamics Conference, St. Louis, Missouri. 2002.

[15] Ali, W., “Aerodynamics of Rotating Disc Wings.” Division of Aerospace, Undergraduate Report, School of Engineering, University of Manchester, UK, April 1998.

[16] “Geobat Flying Saucer, Future Horizons.” 2005. 10 November 2007 <http://www.futurehorizons.net/saucer.htm>

[17] Etkin, B., and Reid, L. Dynamics of Flight: Stability and Control 3rd ed. New York: John Wiley and Sons, Inc, 1996.

[18] Abbott, I., and Von Deonhoff, A. Theory of Wing Sections. New York: Dover Publications, Inc, 1958.

APPENDIX A

COEFFICIENT PLOTS

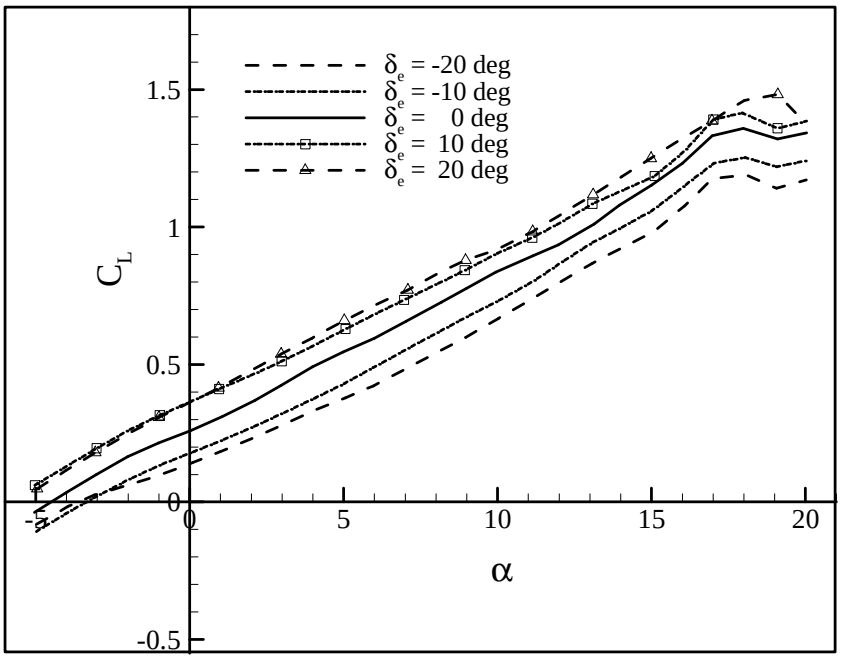

Figure A1: Laminar lift coefficient for δ_F = 10 deg

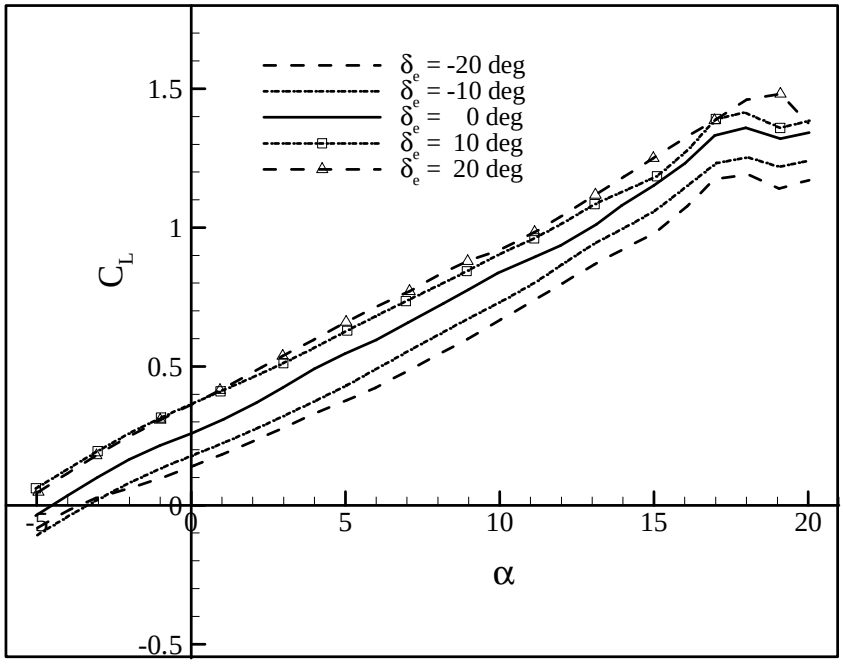

Figure A2: Laminar lift coefficient for δ_F = 20 deg

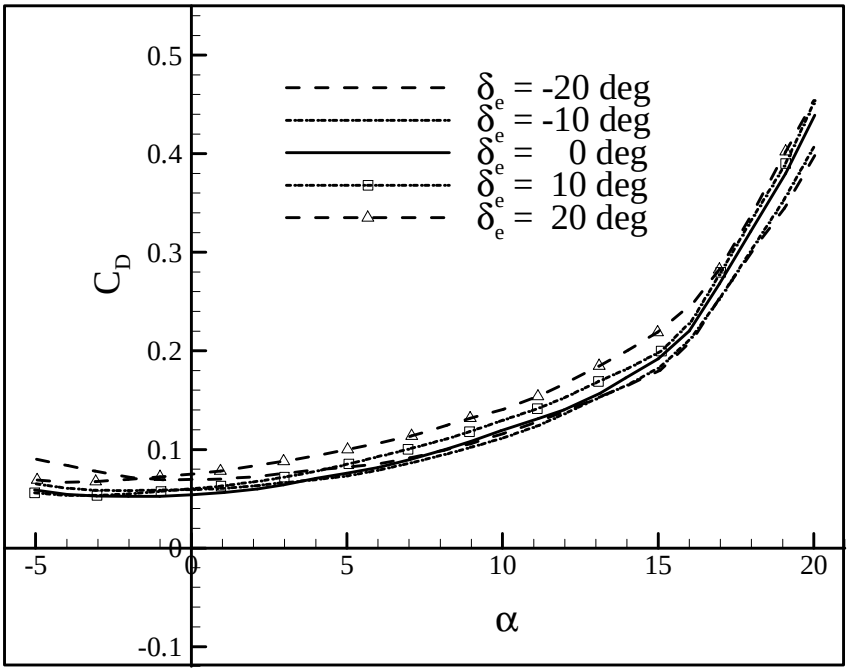

Figure A3: Laminar drag coefficient for δ_F = 10 deg

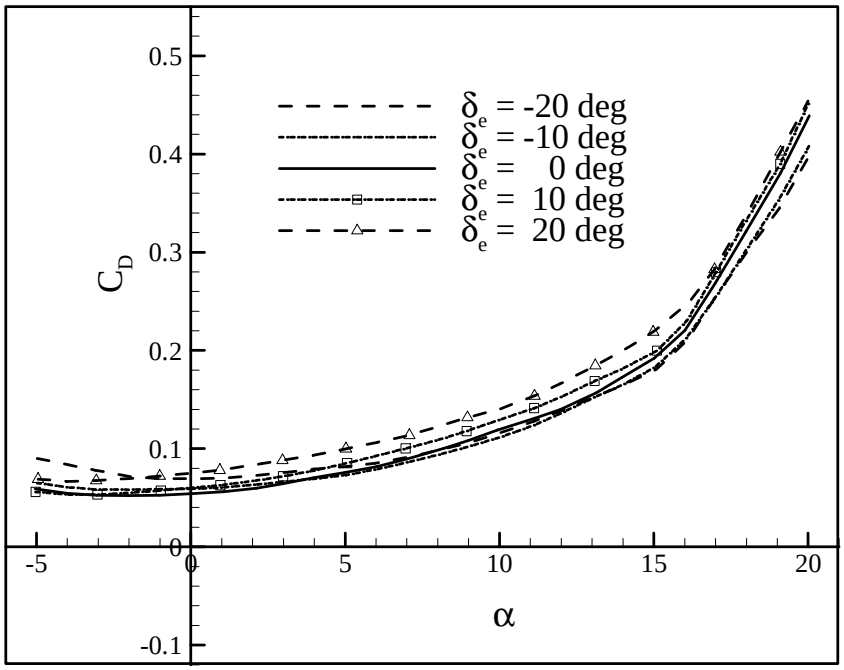

Figure A4: Laminar drag coefficient for δ_F = 20 deg

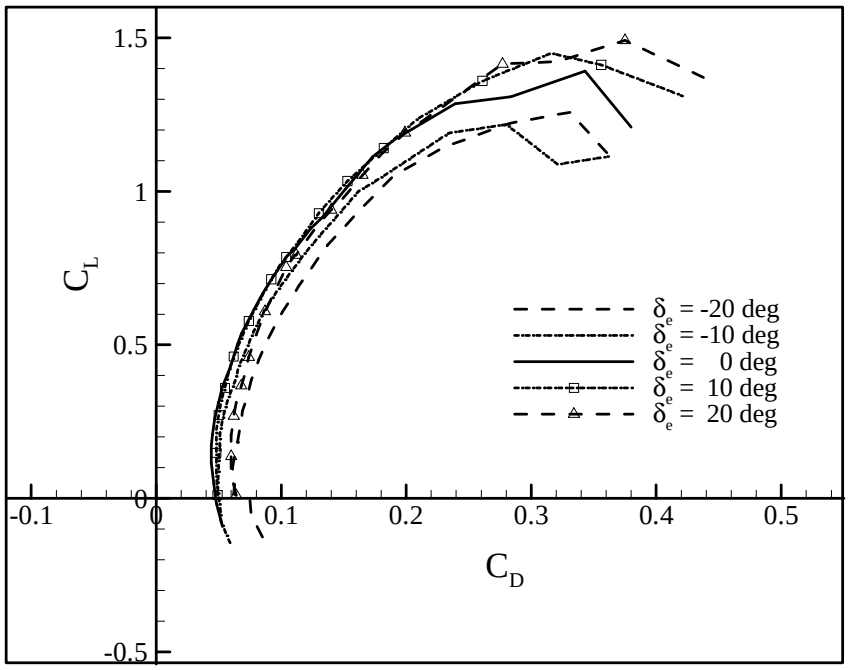

Figure A5: Laminar drag polar for δ_F = 10 deg

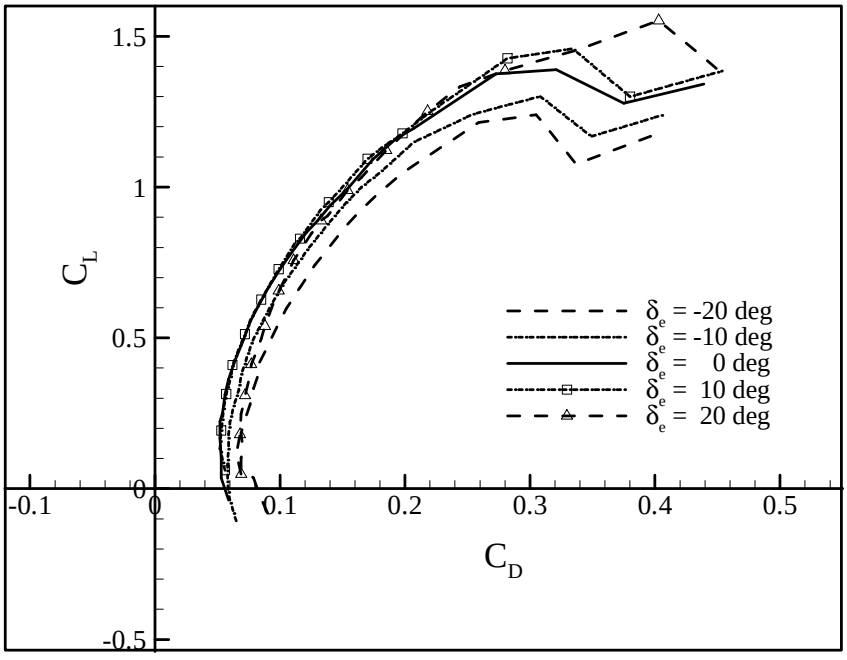

Figure A6: Laminar drag polar for δ_F = 20 deg

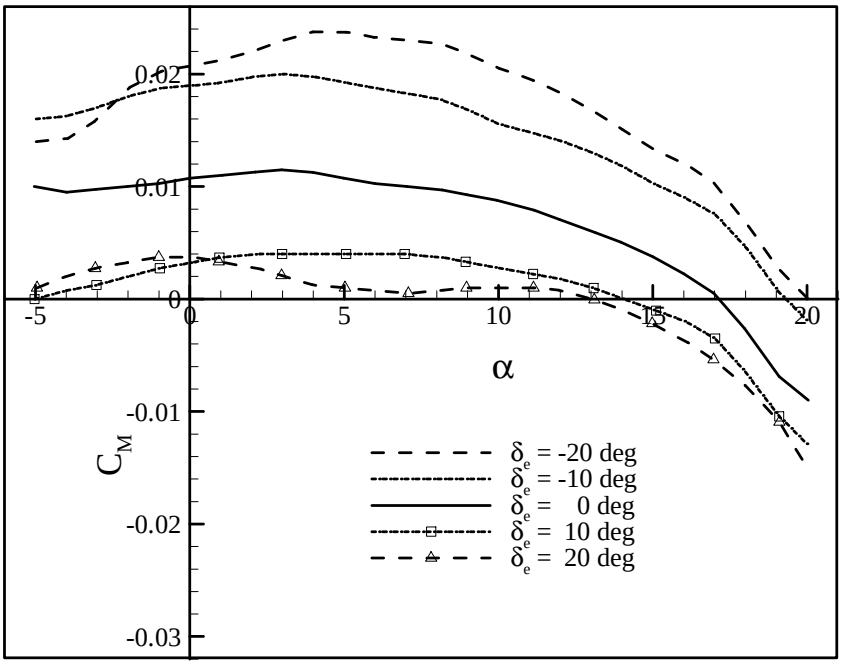

Figure A7: Laminar pitching moment coefficient for δ_F = 20 deg

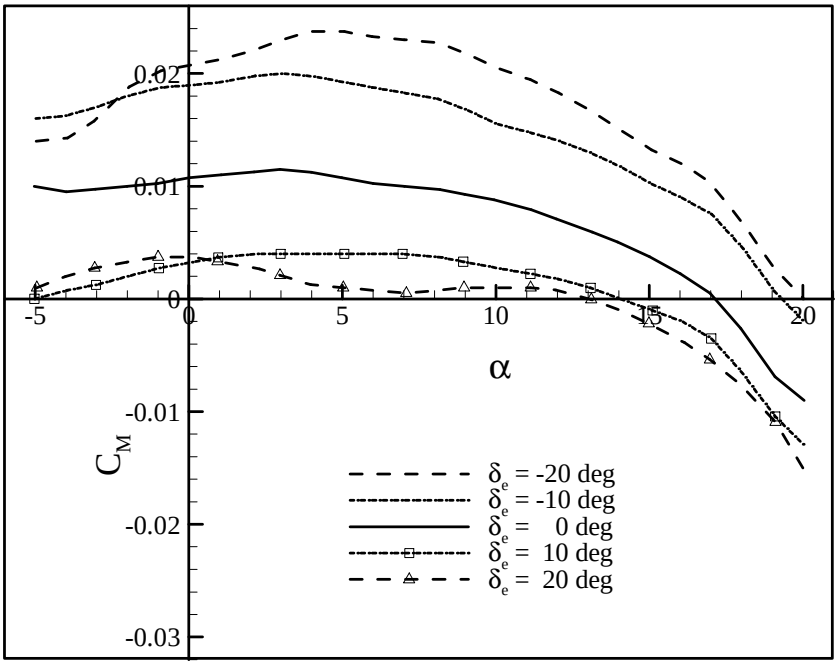

Figure A8: Laminar pitching moment coefficient for δ_F = 20 deg

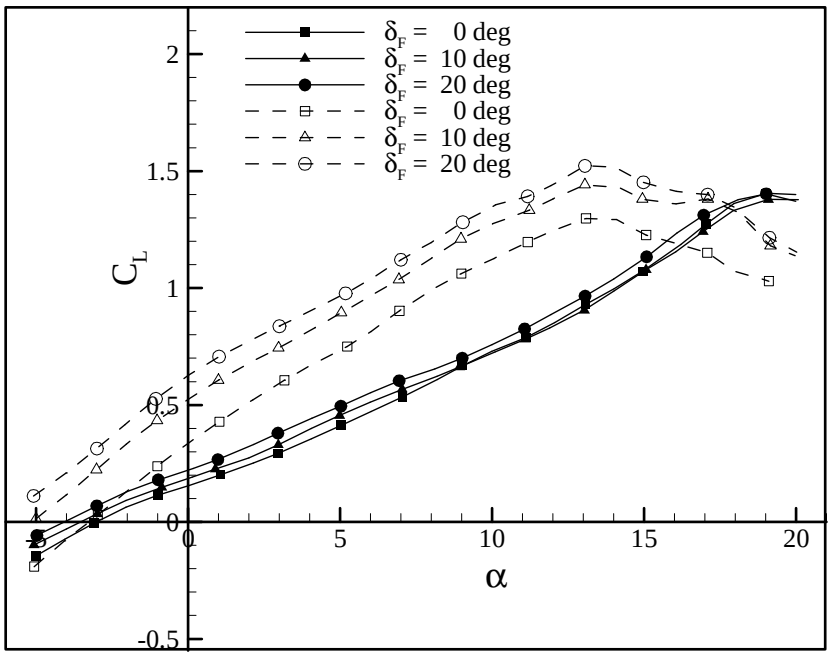

Figure A9: Lift curve- Geobat and Cessna comparison for δ_e = 0 deg; solid symbols- Geobat, open symbols- Cessna 172

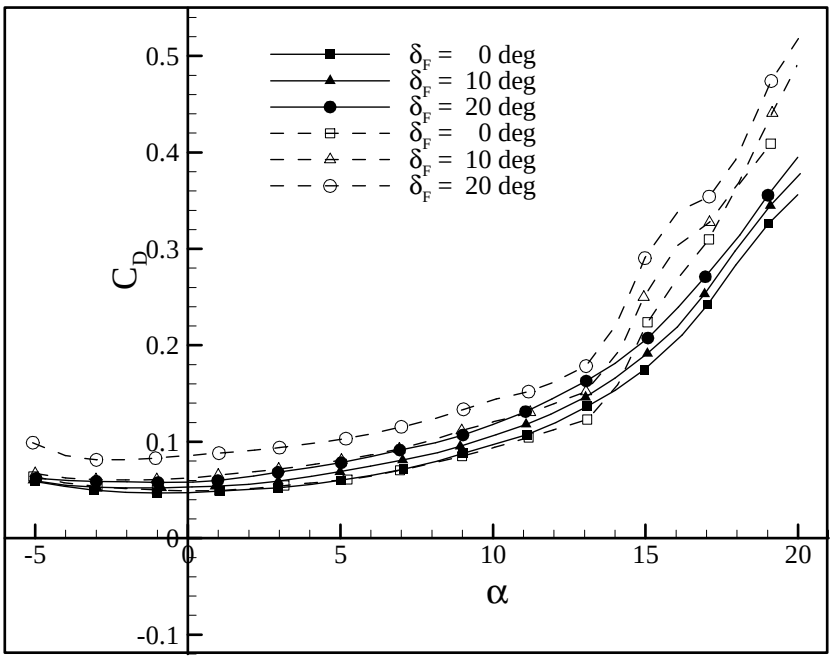

Figure A10: Drag curve- Geobat and Cessna comparison for δ_e = 0 deg; solid symbols- Geobat, open symbols- Cessna 172

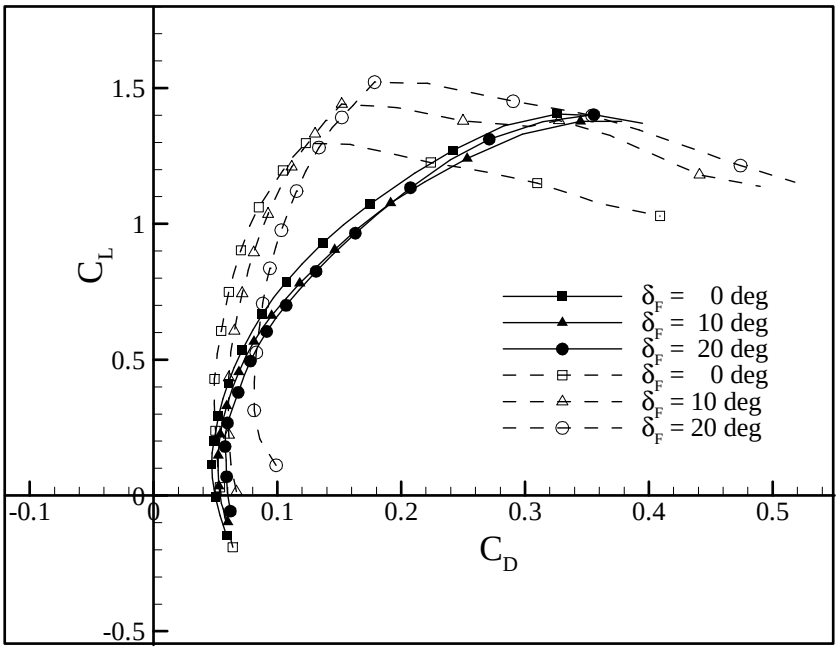

Figure A11: Drag polar curve- Geobat and Cessna comparison for δ_e = 0 deg; solid symbols- Geobat, open symbols- Cessna 172

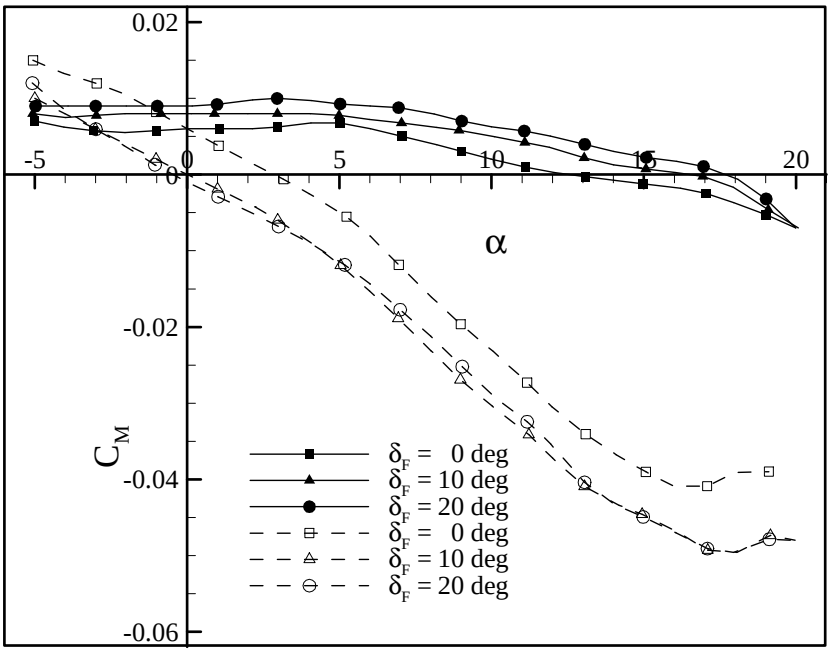

Figure A12: Pitching moment curve- Geobat and Cessna comparison for δ_e = 0 deg; solid symbols- Geobat, open symbols- Cessna 172

APPENDIX B

FLOW VISUALIZATION

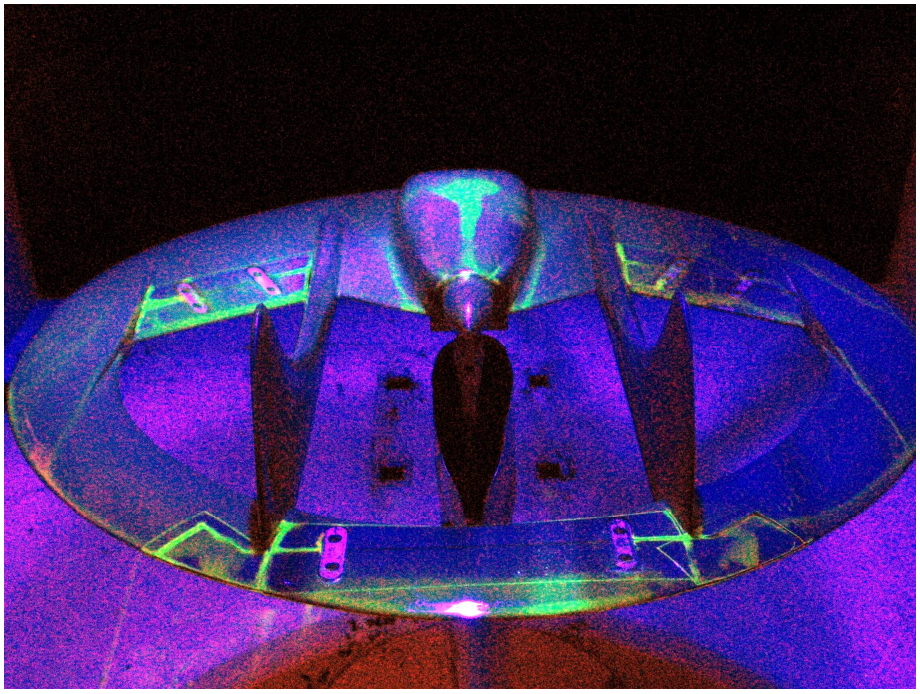

Figure B1: Rear view at α = 0 deg

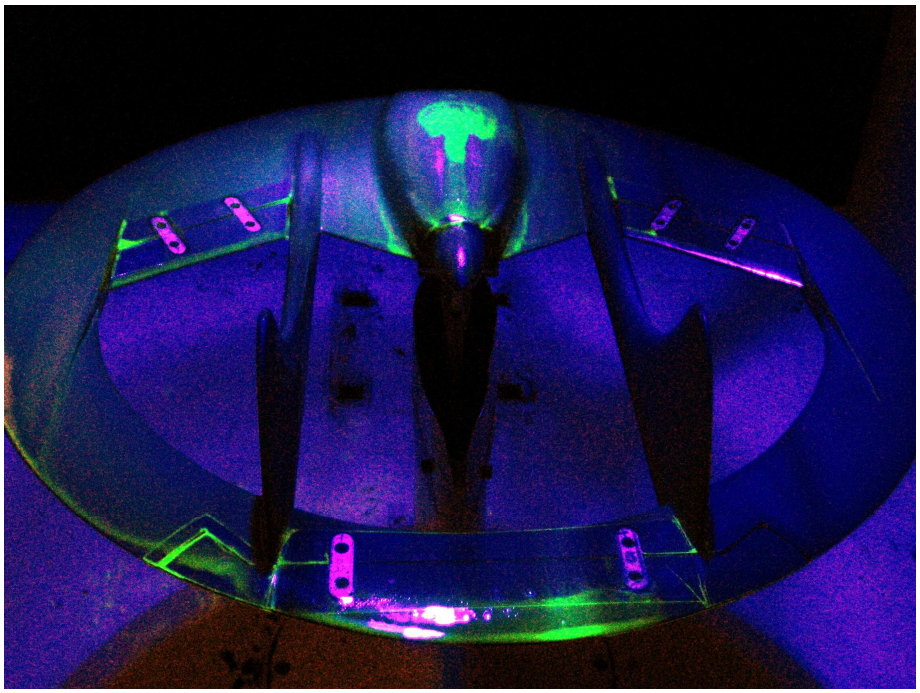

Figure B2: Rear view at α = 0 deg

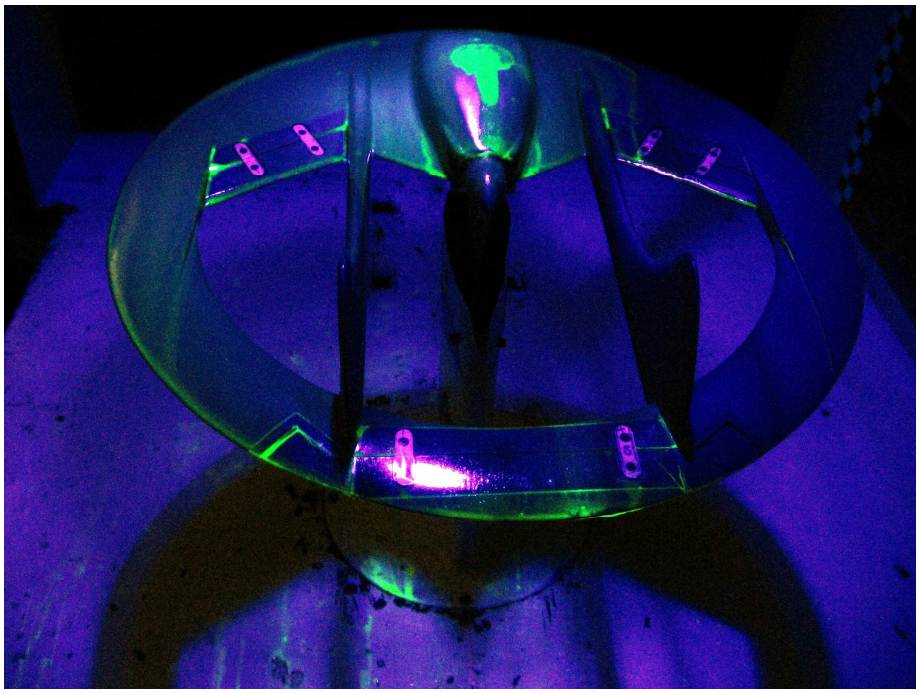

Figure B3: Rear view at α = 5 deg

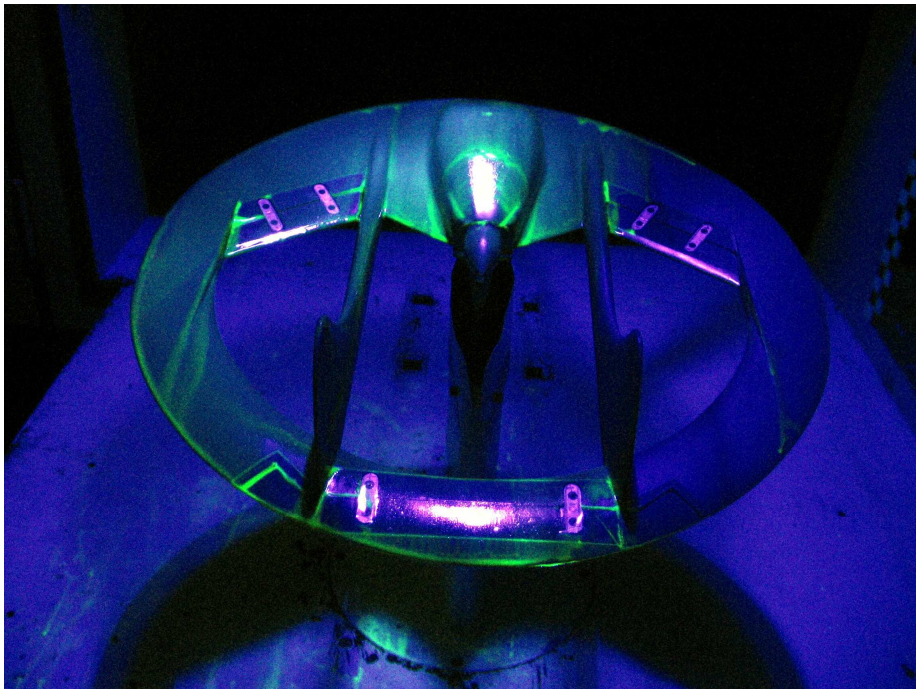

Figure B4: Rear view at α = 10 deg

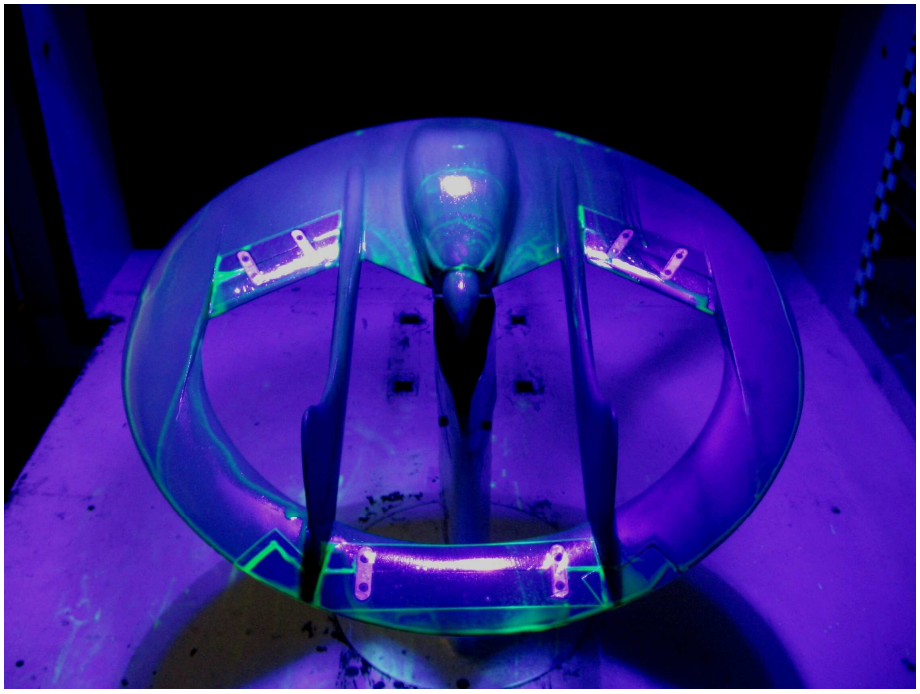

Figure B5: Rear view at α = 15 deg